

Supplementary Methods - General Parameters

Parameter	Value	Application
Reference temperature	37 °C	Nernst / GHK equations
Patch-clamp temperature	34 – 35 °C (measurements of V_{rest} and V_{thr})	Difference < 2 mV relative to 37 °C – negligible
[Cl ⁻] _o (control)	130 mM	Standard ACSF
[K ⁺] _o (control)	3 mM	Standard ACSF
Nernst constants (log10; 37 °C)	K ⁺ = +61.54 mV Cl ⁻ = -61.54 mV	$RT/F \times 2.303$

A Nernst constant of 61.54 mV ($R = 8.314 \text{ J mol}^{-1} \text{ K}^{-1}$, $T = 310 \text{ K}$, $F = 96\,485 \text{ C mol}^{-1}$) was assumed for 37 °C.

Reducing the temperature to 35 °C lowers this constant to 61.12 mV, shifting all calculated equilibrium potentials by $\approx 0.68\%$ ($\approx 0.57 \text{ mV}$) when [Cl⁻]_i = 5.8 mM.

The numerical value 61.54 mV is positive; the “-” sign appears because Cl⁻ carries a negative charge in the equation itself.

2.1 Reduction in KCC2 activity (Ser940 dephosphorylation) — model of the E_{GABA} shift

Chronic restraint stress (CRS) induces a depolarising shift of the GABA_A reversal potential (E_{GABA}) in CA1 measured with gramicidin-perforated patch (MacKenzie and Maguire 2015; Fig. 2C). Independently, KCC2 membrane stability and transport activity are positively regulated by PKC-dependent phosphorylation at Ser940 (Lee et al. 2007) and NMDA receptor activity down-regulates KCC2, thereby promoting depolarising GABA_A currents (Lee et al. 2011). In our modelling we therefore treat the CRS-induced depolarisation of E_{GABA} as the functional consequence of reduced KCC2-mediated Cl⁻ extrusion. We do not claim that Ser940 dephosphorylation under CRS was directly demonstrated in (MacKenzie and Maguire 2015); rather, Ser940 is cited as a mechanistic link explaining how KCC2 regulation can produce an E_{GABA} shift.

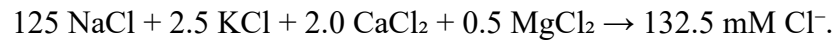
To isolate this mechanism, we describe below only the procedure used to model the shift in E_{GABA} .

2.1.A ACSF recipes & chloride totals (basis for [Cl⁻]_o = 130 mM)

To set a reproducible reference for extracellular chloride we compiled representative hippocampal ACSF recipes and explicitly summed all chloride-bearing salts. A typical ACSF used in mouse CA1 slices contains (in mM): 125 NaCl, 2.5–3.0 KCl, 2.0 CaCl₂, 1.0 MgCl₂, 25 NaHCO₃, 1.25 NaH₂PO₄, 10–25 glucose. Only the halide salts contribute Cl⁻. The total [Cl⁻]_o is therefore:

- 125 mM (from NaCl)
 - (2.5–3.0) mM (from KCl)
 - 4 mM (from 2.0 mM CaCl₂; 2 Cl⁻ per Ca²⁺)
 - 2 mM (from 1.0 mM MgCl₂; 2 Cl⁻ per Mg²⁺)

Examples:



Across commonly used variants (small differences in KCl, CaCl₂, MgCl₂) this yields a practical range of ≈ 128–136 mM. Some protocols substitute MgSO₄ for MgCl₂; in such cases the total [Cl⁻]_o is correspondingly lower, which still falls within our 128–136 mM range. We therefore adopt [Cl⁻]_o = 130 mM as the reference value for all baseline Nernst calculations; sensitivity runs at 128/130/136 mM are reported where relevant. (Buffers such as HEPES/NaHCO₃ and glucose do not contribute Cl⁻.)

Representative ACSF protocols (direct quotes)

Slices were perfused with ACSF containing (in mM): 125 NaCl, 2.5 KCl, 2.0 CaCl₂, 1.3 MgSO₄, 1.25 NaH₂PO₄, 26 NaHCO₃, and 10 glucose, pH 7.4 when bubbled with 95% O₂/5% CO₂ (Diamond 2001).

ACSF contained (in mM): 124 NaCl, 3 KCl, 1.25 NaH₂PO₄, 1.3 MgSO₄, 2 CaCl₂, 26 NaHCO₃, and 10 glucose, bubbled with 95% O₂–5% CO₂ (Cash and Yuste 1999).

ACSF contained (in mM): 125 NaCl, 2.5 KCl, 1.25 NaH₂PO₄, 1 MgCl₂, 2 CaCl₂, 26 NaHCO₃, and 10 glucose, equilibrated with 95% O₂–5% CO₂ (Spruston and Johnston 1992).

Some protocols use MgSO₄ instead of MgCl₂; in such cases the total extracellular chloride is correspondingly lower, consistent with our 128–136 mM range.

2.1.B Hipposeq extraction & vCA1/dCA1 KCC2 ratio (1.03 ± 0.04)

We derived the ventral-to-dorsal expression ratio for SLC12A5 (KCC2) from the Hipposeq RNA-seq resource (Cembrowski et al. 2016b) as follows.

Data scope

- Cell class: CA1 pyramidal neurons (Hipposeq “pyramidal” clusters).
- Regions: dorsal CA1 (dCA1) and ventral CA1 (vCA1) as defined in Hipposeq.

- Measure: TPM values for SLC12A5 across all available replicates per region.

Procedure

1. For each replicate, extract the SLC12A5 TPM.
2. Compute region means (μ_v , μ_d) and standard deviations (σ_v , σ_d) on linear TPM.
3. Report the v/d ratio $r = \mu_v/\mu_d$ and its uncertainty as SD of replicate-level ratios ($v\text{TPM}_i/d\text{TPM}_j$) aggregated within each dataset; for robustness we verified the same conclusion using $\log_2(\text{TPM} + 1)$ with negligible change (< 0.5 %).
4. Outlier handling: no replicate was excluded; results are stable to leave-one-out.

Result

$r = 1.03 \pm 0.04$ (mean \pm SD), indicating no appreciable dorsoventral gradient for KCC2 in CA1 pyramidal neurons. This justifies using dCA1 gramicidin E_{GABA} as the baseline for vCA1 in our modelling (a conservative choice with respect to excitability).

2.1.C Leak-fraction calibration for g_{Cl} and NKCC1 sensitivity (used in 2.1.5)

Purpose

To link an E_{GABA} shift to a somatic V_{rest} change via a physically interpretable coefficient and to bracket the effect of potential NKCC1 up-regulation under CRS.

C1. Calibrating g_{Cl} (fractional chloride contribution to V_{rest})

We model the resting potential as $V_{\text{rest}} = \Sigma(g_i E_i)/\Sigma g_i$. For small shifts in E_{Cl} around baseline ($[Cl^-]_i \approx 5.8 \text{ mM}$), the induced somatic depolarisation is approximately linear:

$$\Delta V_{\text{rest}} \approx g_{\text{Cl}} \Delta E_{\text{GABA}}.$$

We calibrated g_{Cl} by matching the inhibition-efficacy regime reported for CA1 pyramidal neurons (Doyon et al. 2011) dynamic Cl⁻ model under small (5–10 mV) E_{GABA} shifts, while keeping the passive leak budget consistent with classic CA1 models (Booth and Rinzel 1995). This yields $g_{\text{Cl}} = 0.15$ with a conservative uncertainty of ± 0.03 to cover lab-to-lab variability in leak composition. This value is used only when converting ΔE_{GABA} into a V_{rest} contribution (e.g. IL-6/STAT3 pathway) and is not applied when adding the CRS-induced E_{GABA} shift to the excitability margin itself, to avoid double counting.

C2. NKCC1 sensitivity (not in the main scenario)

The main CRS scenario does not include NKCC1 up-regulation. To quantify an upper-bound effect, we increased the NKCC1 component by +25 % in a dynamic chloride framework

(parameterised on Currin & Raimondo 2022) at the reference $[Cl^-]_o$. Under these conditions the additional E_{GABA} depolarisation is $\approx +1$ mV. We treat this as a model result used only in sensitivity notes (2.1.5) and do not add it to the minimal main case.

C3. Uncertainty handling & temperature

Uncertainties from input variance (e.g. digitised E_{GABA} , $[Cl^-]_i$ baseline, g_{Cl}) are combined by root-sum-of-squares. All constants are given for 37 °C (61.54 mV for the \log_{10} Nernst form); at 35 °C the constant is 61.12 mV (≈ 0.68 % lower), shifting E_{GABA} by $\sim 0.6\text{--}0.8$ mV in our baseline—too small to affect conclusions.

2.1.1 Input parameters

Table 2.1 Parameters used in the E_{GABA} shift model

Parameter	Value (mean \pm SD)	Source / provenance
$[Cl^-]_o$ (standard artificial cerebrospinal fluid, ACSF)	130 mM (practical range 128–136 mM total Cl^-)	Representative ACSF protocols; see 2.1.A (ACSF recipes & totals). Our reference value uses 125 mM NaCl as the dominant contributor to extracellular Cl^- ; totals depend on KCl, CaCl ₂ , MgCl ₂ .
$[Cl^-]_i$ (control)	5.8 ± 0.6 mM	Our back-calculation from gramicidin E_{GABA} (MacKenzie and Maguire 2015; Fig. 2C) using Nernst @ 37 °C; details digitisation & uncertainty: 2.1.2 (Digitisation & back-calculation); numeric grid in Supplementary Table S1.
E_{GABA} (control)*	-83.1 ± 1.2 mV	Digitised from Fig. 2C (MacKenzie and Maguire 2015) digitisation & uncertainty: 2.1.2 (Digitisation & back-calculation).
Nernst constant (37 °C, \log_{10})	61.54 mV	RT / F \times 2.303 at 310 K (see 2.1.2).
Relative KCC2 expression (vCA1/dCA1)	1.03 ± 0.04	Our derivation from RNA-seq (Hipposeq; (Cembrowski et al. 2016b; Cembrowski et al. 2016a); RNA-seq extraction & averaging: 2.1.B).
Contribution of G_{Cl} to V_{rest} stabilisation	0.15 ± 0.03	Model parameter (calibrated) consistent with classic leak-fraction budgets (Booth and Rinzel 1995) rationale 2.1.C. (Migliore et al. 2018) cited for variability context, not for this exact fraction.)

* CA1, gramicidin-perforated patch; rescaled to 37 °C; see 2.1.2. In typical transverse slices this corresponds to dorsal segments. Numeric mean/SD are not printed verbatim in the source paper; they are our digitised estimates from Fig. 2C (procedure in 2.1.2 Digitisation & back-calculation).

Notes on ACSF: A typical ACSF (e.g., 125 mM NaCl, 2.5–3 mM KCl, 2 mM CaCl₂, 1 mM MgCl₂) yields a total $[Cl^-]_o$ near 132–134 mM (125 + 2.5–3 + 4 + 2). Across laboratories,

compositions produce ~128–136 mM total Cl⁻. We therefore set [Cl⁻]_o=130 mM as the reference and regard ~128–136 mM as the practical range (see 2.1.A (ACSF recipes & totals) for specific protocol citations).

2.1.2 Equations

At 37 °C:

$$\frac{RT}{F} = 26.70 \text{ mV} \Rightarrow \frac{RT}{F} \times 2.303 = 61.54 \text{ mV.}$$

For chloride (log₁₀ form):

$$E_{Cl} = -61.54 \text{ mV} \times \log_{10} \left(\frac{[Cl^-]_o}{[Cl^-]_i} \right).$$

For comparison, at 35°C (308 K), the constant is 61.12 mV, i.e. ~0.68 % lower; in our baseline this changes E_{GABA} by ≈ 0.6 mV, which does not affect conclusions (see 2.1.5).

Digitisation & back-calculation of E_{GABA} .

Values for E_{GABA} were digitised from Fig. 2C of (MacKenzie and Maguire 2015) after axis calibration to the labelled tick marks; for each condition, several points around the plotted mean were sampled and averaged (values rounded to 0.1 mV). Uncertainty for the control mean was taken as the SD across picks and propagated as described below. Measured E_{GABA} at 35 °C was converted to intracellular chloride using the log₁₀ Nernst form with the temperature-appropriate constant (61.12 mV at 308 K):

$$[Cl^-]_{i,35} = [Cl^-]_o \times 10^{E_{GABA,\text{meas}}/61.12}$$

Temperature rescaling to 37 °C. The same [Cl⁻]_i was then inserted into the 37 °C Nernst equation (constant = 61.54 mV at 310 K):

$$E_{GABA,37} = -61.54 \text{ mV} \times \log_{10} \left(\frac{[Cl^-]_o}{[Cl^-]_{i,35}} \right)$$

In our data this increases E_{GABA} by ≈ 0.6–0.8 mV relative to 35 °C, consistent with the 0.68 % change in the Nernst constant.

Rounding convention. Supplementary Table S1 was computed with 61.50 mV (rounded), to match source conventions; differences vs 61.54 mV are ≤ 0.06 mV and have no impact on ΔE_{GABA} .

Reproducibility. The complete numeric grid (5.0–8.0 mM) is provided in Supplementary Table S1.

2.1.3 Calculation procedure

1. Define the reference state Set baseline values $[Cl^-]_i$, $[Cl^-]_o$ and the calculated $E_{GABA,ctrl}$.
2. Introduce the perturbation Assign a new intracellular chloride concentration, $[Cl^-]_{i,test}$, corresponding to the desired reduction in KCC2 activity.
3. Compute the shift

$$\Delta E_{GABA} = E_{Cl,CRS} - E_{Cl,ctrl}$$

4. Inverse equation (estimate $[Cl^-]_i$)

$$[Cl^-]_{i,CRS} = [Cl^-]_{i,ctrl} 10^{\Delta E_{GABA}/61.54}$$

5. Error propagation Uncertainties were combined by root-sum-of-squares (see 2.5.5).

Worked example (our calculation): For $\Delta E_{GABA} = +8.25$ mV baseline $[Cl^-]_i = 5.8$ mM $[Cl^-]_{i,CRS} = 7.9$ mM. The full grid (5.0–8.0 mM) is provided in Supplementary Table S1.

Note: The +8.2 mV value used for vCA1 is an extrapolation based on (i) the measured CRS-induced E_{GABA} shift in CA1 (gramicidin-perforated patch), (ii) the absence of a significant KCC2 dorsoventral gradient in CA1 (Hipposeq), and (iii) the conservative convention of using the CA1 value as a lower bound for vCA1.

2.1.4 Sensitivity analysis

- Analysed range: $[Cl^-]_i = 5–8$ mM.
- Additional sensitivity to $[Cl^-]_o$: results are reported for 128, 130, 136 mM.
- The full results matrix is presented in Supplementary Table S1.

2.1.5 Methodological notes

CA1 → vCA1 extrapolation. Baseline E_{GABA} values were measured in CA1 (MacKenzie and Maguire 2015). We extrapolated to ventral CA1 (vCA1) because RNA-seq (Cembrowski et al. 2016b; Cembrowski et al. 2016a) shows no appreciable dorsoventral gradient for SLC12A5/KCC2 (our v/d ratio = 1.03 ± 0.04 ; 2.1.B. Moreover, intrinsic excitability and several conductances differ along the dorsoventral axis (e.g., (Dougherty et al. 2012; Marcellin et al. 2012; Miliar et al. 2016; Malik and Johnston 2017), often rendering vCA1 more excitable. Treating dCA1 E_{GABA} as the baseline for vCA1 is therefore conservative with respect to the likelihood that a given depolarisation narrows the excitability margin.

NKCC1 was not included in the main scenario. Potential up-regulation of NKCC1 after CRS was not modelled in the main case. In our sensitivity analysis (2.1.C), a +25 % increase of the NKCC1 component yielded an additional $\approx +1$ mV depolarisation of E_{GABA} under reference parameters — this is our model result. We cite (Currin and Raimondo 2022) for theoretical background on chloride dynamics, not for this specific number.

Parameter origins.

- KCC2 v/d = 1.03 ± 0.04 — our derivation from Hipposeq (Cembrowski et al. 2016b; Cembrowski et al. 2016a); extraction, replicates and averaging in 2.1.B.
- $G_{\text{Cl}}/\sum G_{\text{leak}} = 0.15 \pm 0.03$ — model calibration guided by (Doyon et al. 2011); full derivation in 2.1.C. This value is not quoted verbatim in Doyon et al.; we report it transparently as a calibrated parameter.
- ACSF chloride: the range 128–136 mM total $[\text{Cl}^-]_o$ follows from standard ACSF recipes; concrete protocol citations are listed in 2.1.A.

Temperature. Values are reported at 37 °C. At 34–35 °C the Nernst constant is ~ 0.68 % smaller (61.12 mV at 35 °C), shifting all equilibrium potentials by ~ 0.6 –0.8 mV in our baseline; this does not affect conclusions.

Rounding in the main text. In Table 3.1 we report a conservative $\Delta E_{\text{GABA}} = +8.2$ mV rounded down from +8.25 mV (propagated RSS uncertainty ≈ 0.2 –0.3 mV).

GABA_A channels also pass

$$P_{\text{HCO}_3^-}/P_{\text{Cl}^-} \approx 0.2$$

which offsets absolute E_{GABA} by a few mV; because $[\text{HCO}_3^-]$ is assumed constant across conditions, the ΔE_{GABA} arising from changes in $[\text{Cl}^-]_i$ is, to first order, equal to ΔE_{Cl} used here (Kaila 1994; Voipio and Kaila 2000).

2.2 Reduction in Kir4.1 conductance and extracellular space shrinkage — model of $[\text{K}^+]_o$ elevation

A reduction in extracellular space (ECS) together with impaired astrocytic K^+ uptake (e.g., via Kir4.1) worsens K^+ buffering. Under chronic restraint stress (CRS) these processes facilitate transient or tonic increases in extracellular potassium, $[\text{K}^+]_o$, which shift E_K and depolarise V_{rest} . In the model we parameterise the *net* effect via $\Delta[\text{K}^+]_o$ without assigning molecular

weights. Below we document only the numerical procedure; quantitative outcomes are reported in the Results.

2.2.1 Input parameters

Table 2.2 Parameters used in the $[K^+]$ _o elevation model

Parameter	Value (mean \pm SD)	Source
$[K^+]$ _o at rest (CA1)	3.00 ± 0.10 mM	In vivo CA1 baseline and classic physiology (Krnjević et al. 1982); matches standard ACSF (3 mM KCl).
$\Delta[K^+]$ _o in wakefulness	$+0.40 \pm 0.05$ mM	(Ding et al. 2016) cortex; used here as a physiological reference magnitude for wakefulness-related tonic rises.
Transient “K ⁺ burst” (upper-bound sensitivity case)	$+3.00 \pm 0.20$ mM	Conservative, non-pathological upper bound consistent with stimulation-evoked increases reported in hippocampus (Krnjević et al. 1982). Not calibrated on hypoxic depolarisation.
Nernst constant for K ⁺ (37 °C, log ₁₀)	61.54 mV	RT/F \times 2.303 at 310 K (as in 2.1.2).
Fractional K ⁺ conductance in V_{rest} (f_K)	0.15 ± 0.03 (range 0.15–0.25 in sensitivity)	Lower-bound K ⁺ fraction in leak budgets from neuron-extracellular-glia models (Sætra et al. 2021); Table 1. Range extended to 0.25 to cover models with stronger $I_{K(\text{leak})}$ (Halnes et al. 2016; Migliore et al. 2018).

Rationale/notes.

Baseline $[K^+]$ _o = 3.0 mM is the canonical resting value near CA1 (Krnjević et al. 1982) and coincides with standard ACSF. The wakefulness rise $\approx +0.4$ mM is anchored to (Ding et al. 2016), who quantified state-dependent interstitial ion changes (we use it as a physiological reference magnitude). The “burst” case +3 mM is a conservative, strong-but-non-pathological increment consistent with stimulation-evoked hippocampal K⁺ elevations (Krnjević et al. 1982); it is not derived from hypoxic spreading depolarisation (HSD). The f_K parameter is a scaling coefficient in a parallel-conductance picture; we adopt 0.15 ± 0.03 as a conservative lower bound from models with explicit ECS and glia (Sætra et al. 2021) and test 0.15–0.25 to cover stronger K⁺ leak implementations (Halnes et al. 2016; Migliore et al. 2018).

2.2.2 Equations

1. Shift in the K⁺ equilibrium potential

$$\Delta E_K = 61.54 \text{ mV} \times \log_{10} \left(\frac{3 + \Delta [K^+]_o}{3} \right).$$

2. Impact on the resting potential

$$\Delta V_{\text{rest}} = f_K \Delta E_K,$$

where f_K is the fraction of total membrane conductance carried by K^+ channels.

(Temperature note: at 35 °C the \log_{10} Nernst constant is 61.12 mV; the ≈ 0.68 % difference shifts ΔE_K by < 1 % and is negligible for our conclusions.)

2.2.3 Calculation procedure

1. Define baseline conditions Set $[K^+]_o = 3.00$ mM and the nominal f_K from Table 2.2.
2. Specify change scenarios Introduce $\Delta[K^+]_o$ representing:
 - (i) a moderate tonic rise during wakefulness (+0.35–0.40 mM),
 - (ii) short-lived “ K^+ bursts” linked to strong network activity (up to +3.0 mM).
3. Compute ΔE_K . Insert the chosen $\Delta[K^+]_o$ into the ΔE_K equation.
4. Determine ΔV_{rest} . Multiply the resulting ΔE_K by f_K .
5. Error propagation The standard error, $\sigma_{\Delta V}$, was obtained by root-sum-of-squares (see 2.5.5).

An illustrative example ($\Delta[K^+]_o = +0.35$ mM → ΔE_K , ΔV_{rest}) is provided in Supplementary Table S2.

2.2.4 Sensitivity analysis

- Analysed range: $\Delta[K^+]_o = 0.2$ –3.5 mM and $f_K = 0.15$ –0.25. The full ΔV_{rest} matrix is presented in Supplementary Table 2.

2.2.5 Methodological notes

- Mechanism aggregation. CRS is associated with reduced ECS and lower Kir4.1, both favouring K^+ accumulation; we parameterise the net effect via $\Delta[K^+]_o$ without assigning relative weights (Schnell et al. 2012).
- Wakefulness rise is negligible for the budget. A tonic +0.40 mM produces $\Delta V_{\text{rest}} \approx 0.5$ mV for $f_K = 0.15$, i.e. below typical RMP resolution; we treat it as negligible in the cumulative depolarisation budget (Ding et al. 2016).
- “ K^+ bursts” kept separate from P2X7. We consider transient $\Delta[K^+]_o$ up to +3 mM as a sensitivity case for strong network activity and analyse it separately from P2X7-driven depolarisation (2.5) to avoid double counting.

- No calibration on HSD. (Schnell et al. 2012) directly showed that CRS reduces ECS and accelerates interstitial K^+ accumulation during hypoxia; we therefore treat $\Delta[K^+]$ as an aggregate parameter. Reduced Kir4.1 activity is cited as a plausible contributor to impaired K^+ clearance (Sibille et al. 2014; Méndez-González et al. 2020), but we do not assume a specific Kir4.1 change in the baseline calculation.
- Fractional K^+ conductance (f_K). We adopt $f_K = 0.15 \pm 0.03$ as a conservative lower bound from ECS/glia-aware models (Sætra et al. 2021) and test up to 0.25 to cover variants with stronger K^+ leak (Halnes et al. 2016; Migliore et al. 2018).

2.3 Interleukin-6 elevation — reduced KCC2 activity and NKCC1 induction

In CA1 neurons IL-6 signals via the IL-6R/gp130 → JAK/STAT3 cascade (Hu et al. 2022). Related work shows that cytokine/BDNF-like signalling can down-regulate KCC2 and, in some preparations, promote NKCC1 up-regulation (Rivera et al. 2002; Rivera et al. 2004; Pieraut et al. 2011), thereby increasing intracellular Cl^- , depolarising E_{GABA} , and narrowing the $V_{rest} \rightarrow V_{thr}$ margin.

2.3.1 Input parameters

Table 2.3 Parameters used in the IL-6 → KCC2 / NKCC1 model

Parameter	Value (mean \pm SD)	Source / notes
IL-6 elevation after chronic stress (hippocampus)	—	(Li et al. 2008; Zhang et al. 2016) reported increase; qualitative anchor, value not used numerically
IL-6 trans-signalling in CA1 neurons	—	(Hu et al. 2022)
KCC2 reduction (surrogate for IL-6)	$40 \pm 5\%$	(Rivera et al. 2002; Rivera et al. 2004) BDNF/activity; gramicidin; used as a conservative surrogate for the scale of KCC2 loss
ΔE_{GABA} at 40 % KCC2 loss (surrogate)	$+10.1 \pm 1.3$ mV	Extrapolated from (Rivera et al. 2002; Rivera et al. 2004) (see 2.3.5)
NKCC1 increase after IL-6 (mechanistic)	$+35\%$	(Pieraut et al. 2011) DRG; mechanistic surrogate; used only in sensitivity
Nernst constant for Cl^- ($37^\circ C$, \log_{10})	61.54 mV	$RT / F \times 2.303$ as in 2.1.2
Contribution of G_{Cl} to V_{rest} stabilisation (g_{Cl})	0.15 ± 0.03	calibration as in 2.1.C (context: Doyon et al. 2011; Migliore et al. 2018)

2.3.2 Equations

1. **E_{GABA} shift.** For a given reduction in KCC2, ΔE_{GABA} values are taken directly from (Rivera et al. 2002; Rivera et al. 2004) (gramicidin-perforated patch).

2. Impact on the resting potential

$$\Delta V_{\text{rest}} = g_{\text{Cl}} \Delta E_{\text{GABA}},$$

where $g_{\text{Cl}} = 0.15 \pm 0.03$.

2.3.3 Calculation procedure

1. **Reference scenario** Assume a 40 % loss of KCC2 (robust IL-6/STAT3 activation).
2. **E_{GABA} shift.** Use $\Delta E_{\text{GABA}} \approx +10.1 \text{ mV}$ (surrogate from **Rivera et al.**).
3. **Compute ΔV_{rest}**

$$\Delta V_{\text{rest}} \approx 0.15 \Delta E_{\text{GABA}} \approx +1.5 \text{ mV}$$

4. **Error propagation** Standard uncertainty was combined by the root-sum-of-squares rule (see S2.5.5).

The complete ΔV_{rest} matrix for 20–50 % KCC2 loss is provided in Supplementary Table 3.

2.3.4 Sensitivity analysis

- **KCC2 loss 20–50 %** → $\Delta E_{\text{GABA}} = +5.1 - +12.6 \text{ mV}, \quad \Delta V_{\text{rest}} = +0.8 - +1.9 \text{ mV}$ ($g_{\text{Cl}} = 0.15$).
- **NKCC1 component (sensitivity only).** A +25 % increase in NKCC1 activity adds $\approx +1 \text{ mV}$ depolarisation, estimated in a dynamic chloride framework (Currin and Raimondo 2022). This term is **not** included in the main scenario.

2.3.5 Methodological notes

- Stress → IL-6 in hippocampus. We anchor the cytokine increase to (Zhang et al. 2016) (CUMS; hippocampus).
- Scale of ΔE_{GABA} (surrogate). Direct gramicidin measurements of IL-6-induced ΔE_{GABA} in CA1 are not available; therefore, we use the BDNF/activity-driven KCC2 down-regulation from (Rivera et al. 2002; Rivera et al. 2004) as a conservative surrogate for the magnitude of ΔE_{GABA} at comparable KCC2 loss.
- NKCC1. The +35 % NKCC1 increase from (Pieraut et al. 2011) (DRG) is treated purely as a mechanistic upper-bound and appears only in sensitivity notes; it does not contribute to the main estimate.
- Separation from Ser940 dephosphorylation. The IL-6/STAT3 pathway is treated independently from rapid Ser940 dephosphorylation (2.1). Partial pathway convergence

via BDNF/TrkB is noted qualitatively (Medina et al. 2014; Kitayama 2020) and does not alter the conservative arithmetic used here.

- Linear update rule. For small changes we use $\Delta V_{\text{rest}} = g_{\text{Cl}} \Delta E_{\text{GABA}}$. If future data show larger ΔE_{GABA} in vCA1 (e.g., +12 mV), ΔV_{rest} updates linearly.

2.4 Reduced GIRK and TASK conductance — model of V_{rest} depolarisation

G-protein-activated inwardly rectifying K⁺ channels (GIRK/Kir3.x) and TASK-family two-pore K⁺ channels (K2P 3.1/9.1) are major contributors to the passive K⁺ leak in CA1 pyramidal neurons (Talley et al. 2001; Chen and Johnston 2005). Chronic restraint stress (CRS) reduces functional GIRK influence in ventral CA1 (vCA1) (Malik and Johnston 2017) and, unlike dorsal CA1 (dCA1), there is no demonstrated I_h up-regulation under stress in vCA1 (contrast: (Kim et al. 2018) for dCA1). We therefore estimate the net depolarisation of the resting membrane potential (V_{rest}) expected from diminished GIRK/TASK leak in vCA1. Below we document only the numerical procedure; quantitative outcomes appear in the Results.

2.4.1 Input parameters

Table 2.4 Parameters used in the GIRK/TASK conductance-loss model

Parameter	Value (mean \pm SD)	Source / Note
ΔV_m after Ba ²⁺ block in dCA1 (Ba ²⁺ -sensitive GIRK component)	+0.90 \pm 0.86 mV	(Kim and Johnston 2015) computed as (5.70 \pm 0.70) – (4.80 \pm 0.50) mV to isolate the GIRK-dependent depolarisation (see 2.4.5)
GIRK conductance ratio vCA1 / dCA1	0.35 \pm 0.07	(Malik and Johnston 2017) Fig. 3–5 (range \approx 0.30–0.40 for Ba ²⁺ /TPN-sensitive components)
Input-resistance ratio $R_{\text{in},v} / R_{\text{in},d}$	1.50 \pm 0.20	(Marcelin et al. 2012) (juvenile → conservative); consistent with adult dorsoventral differences (Dougherty et al. 2012; Milior et al. 2016)
TASK contribution relative to GIRK current (assumption)	$f_{\text{TASK}} = 0.25$	(Torborg et al. 2006) (TASK-like component in hippocampus; barium-insensitive), (Talley et al. 2001; Aller and Wisden 2008) (KCNK distribution). No direct adult CA1 pyramidal quantification → treated as a modelling assumption with linear sensitivity.

Notes.

Ba²⁺ at 50 μM blocks Kir/GIRK but spares TASK-like K2P channels (Torborg et al. 2006), hence we add the TASK fraction explicitly. R_{in} ratios above are used as scaling because identical current changes produce larger voltage deflections in cells with higher R_{in} .

2.4.2 Equations

- Scaling dCA1 → vCA1 (GIRK component)

$$\Delta V_{\text{scaled}} = \Delta V_d \left(\frac{R_{\text{in},v}}{R_{\text{in},d}} \right) \left(\frac{g_{\text{GIRK},v}}{g_{\text{GIRK},d}} \right).$$

- Including a TASK fraction (barium-insensitive)

$$\Delta V_{\text{GIRK/TASK}} = \Delta V_{\text{scaled}} (1 + f_{\text{TASK}}),$$

With $f_{\text{TASK}} \approx 0.25$.

- Propagation of total error

$$\sigma_{\Delta V} = \Delta V_{\text{scaled}} \sqrt{\left(\frac{\sigma_R}{R} \right)^2 + \left(\frac{\sigma_g}{g} \right)^2 + \left(\frac{\sigma_f}{1 + f_{\text{TASK}}} \right)^2}$$

(added in quadrature with the scaled baseline SD).

2.4.3 Calculation procedure

- Baseline value $\Delta V_d = 0.90$ mV (Kim and Johnston 2015).
- Scale to vCA1 using $R_{\text{in},v} / R_{\text{in},d} = 1.50$ and $g_{\text{GIRK},v} / g_{\text{GIRK},d} = 0.35$.
- Add the TASK component Multiply by $(1 + f_{\text{TASK}}) = 1.25$.
- Compute $\sigma_{\Delta V}$. Propagate both the baseline uncertainty of ΔV_d and the scaling-factor uncertainties. The baseline error (0.86 mV) is multiplied by the same scaling factor $1.50 \times 0.35 \times (1 + 0.25) = 0.656$, giving $0.86 \times 0.656 \approx 0.56$ mV. Adding the scaling-factor contribution (~ 0.14 mV) in quadrature yields $\sigma_{\Delta V} \approx \sqrt{(0.56^2 + 0.14^2)} \approx 0.58$ mV.

A detailed spreadsheet is provided in Supplementary Table S4.

2.4.4 Sensitivity analysis

- Examined range: $g_{\text{GIRK},v} / g_{\text{GIRK},d} = 0.30 - 0.40$ and $R_{\text{in},v} / R_{\text{in},d} = 1.30 - 1.70$.
- Resulting ΔV_{rest} lies between +0.44 and +0.77 mV (with no I_h compensation). The full value matrix is given in Supplementary Table 4.

2.4.5 Methodological notes

- What ΔV_d represents. The 0.90 ± 0.86 mV value is the difference between Ba^{2+} -sensitive depolarisation with vs. without tonic A₁AR activity ((Kim and Johnston 2015), Tables/Figs 7–8), isolating the GIRK-specific contribution.

- dorsal→ventral scaling. vCA1 has higher R_{in} (Dougherty et al. 2012; Marcellin et al. 2012; Milior et al. 2016) and weaker GIRK influence (Malik and Johnston 2017); we combine both ratios to scale ΔV .
- I_h compensation. CUS/CRS up-regulates I_h in dCA1 (Kim et al. 2018). Comparable compensation has not been demonstrated in vCA1; we therefore present values without I_h counter-depolarisation. If future data show I_h up-regulation in vCA1, the net ΔV_{rest} would be smaller than our estimate.
- TASK assumption. Because TASK-like K2P channels are largely Ba^{2+} -insensitive (Torborg et al. 2006), we include an additional leak fraction f_{TASK} . The main text adopts 0.25 as a transparent assumption supported by KCNK expression/distribution (Talley et al. 2001; Aller and Wisden 2008); ΔV scales linearly with $1 + f_{TASK}$.
- Conservativeness. The chosen GIRK v/d ratio (0.35) is near the upper bound reported by (Malik and Johnston 2017); using a higher value would overestimate ΔV by at most ~0.1 mV across our R_{in} range, i.e. still within the stated uncertainty.

2.5 Microglial Na^+/K^+ -ATPase $\alpha 1$ loss → P2X7-receptor activation

Degradation of the $\alpha 1$ subunit of the Na^+/K^+ -ATPase (NKA- $\alpha 1$) in microglia impairs extracellular- K^+ uptake and increases ATP release, which secondarily activates ionotropic P2X7 receptors (P2X7R) on nearby CA1 neurons. The resulting P2X7R current is depolarising and adds to the V_{rest} shift produced by the concomitant rise in $[K^+]_o$. Below we document the numerical procedure only; quantitative outcomes are reported in the Results.

2.5.1 Input parameters

Table 2.5 Parameters used in the NKA $\alpha 1 \rightarrow$ P2X7R model

Parameter	Value (mean \pm SD)	Source / note
$[K^+]_o$ at rest (CA1)	3.00 ± 0.10 mM	Canonical hippocampal baseline; consistent with standard ACSF and classic CA1 physiology (e.g., (Krnjević et al. 1982)).
Tonic $\Delta [K^+]_o$ under stress/wakefulness (upper bound for subtraction)	$+0.35 \pm 0.05$ mM	Upper end of tonic rises reported across hippocampal/cortical preparations under stress/wakefulness (Schnell et al. 2012; Ding et al. 2016). Used to make the P2X7R-only estimate conservative.
Nernst constant for K^+ ($37^\circ C$, \log_{10})	61.54 mV	$RT/F \times 2.303$ at 310 K (as in 2.1.2).
Fractional K^+ conductance in V_{rest} (f_K)	0.15 ± 0.03	Same conservative leak-budget coefficient used in 2.2 (parallel-

		conductance model; sensitivity carried to 0.25).
ΔV_m in vHIP neurons (mature granule cells) under CRS with microglial NKA- $\alpha 1$ disruption:	$+1.47 \pm 0.18$ mV	digitized from ((Huang et al. 2024 Fig. 2) RMP panels; details in S2.5.5).

Rationale. We re-use $[K^+]_o = 3.0$ mM to maintain internal consistency across modules. For the tonic $\Delta[K^+]_o$ we deliberately take the upper physiological/stress-linked value (+0.35 mM) so that, when we subtract the K^+ -mediated depolarisation, the residual P2X7R-only contribution becomes a lower bound. f_K is the same conservative coefficient as in 2.2 to keep the K^+ contribution maximised, again biasing the residual P2X7R estimate downward.

2.5.2 Equations

- Shift in the K^+ equilibrium potential

$$\Delta E_K = 61.54 \text{ mV} \times \log_{10} \left(\frac{3.00 + \Delta[K^+]_o}{3.00} \right).$$

- K^+ contribution to V_{rest} (parallel-conductance model)

$$\Delta V_{\text{rest}}(K) = f_K \Delta E_K.$$

- Pure P2X7R effect

$$\Delta V_{\text{rest}}(\text{P2X7R}) = \Delta V_m(\text{NKA-}\alpha 1 \text{ disruption}) - \Delta V_{\text{rest}}(K).$$

(Temperature note: at 35 °C the \log_{10} Nernst constant is 61.12 mV; the ~0.68 % difference perturbs ΔE_K by < 1 % in our ranges.)

2.5.3 Calculation procedure

- Compute ΔE_K for $\Delta[K^+]_o = +0.35$ mM:

$$\Delta E_K = 61.54 \text{ mV} \times \log_{10} \left(\frac{3.35}{3.00} \right) \approx +2.95 \text{ mV}.$$

- K^+ contribution to V_{rest} ($f_K = 0.15$):

$$\Delta V_{\text{rest}}(K) = 0.15 \times 2.95 \text{ mV} \approx +0.44 \text{ mV}.$$

- P2X7R-only depolarisation (subtract K^+ component from the in-vivo shift):

$$\Delta V_{\text{rest}}(\text{P2X7R}) = 1.47 \text{ mV} - 0.44 \text{ mV} \approx +1.03 \text{ mV}.$$

- Uncertainty propagation.

For $\Delta V_{\text{rest}}(K) = f_K \Delta E_K$ with $f_K = 0.15 \pm 0.03$ and $\Delta[K^+]_o = 0.35 \pm 0.05$ mM

$$\frac{\partial \Delta E_K}{\partial \Delta[K^+]_o} = \frac{61.54}{\ln 10} \cdot \frac{1}{3.00 + \Delta[K^+]_o} \approx 7.98 \text{ mV} \cdot \text{mM}^{-1}$$

$$\sigma_{\Delta V(K)} \approx \sqrt{\left(\Delta E_K \sigma_{f_K}\right)^2 + \left(f_K \frac{\partial \Delta E_K}{\partial \Delta [K^+]_o} \sigma_{\Delta [K^+]_o}\right)^2} \approx 0.11 \text{ mV}$$

Combine with the in-vivo SD (0.18 mV) in quadrature:

$$\sigma_{\Delta V(P2X7R)} \approx \sqrt{0.18^2 + 0.11^2} \approx 0.21 \text{ mV}$$

Result used downstream. We adopt +1.0 mV (rounded down) as the conservative P2X7R contribution in the cumulative depolarisation budget; note that our explicit estimate is $+1.03 \pm 0.21$ mV.

A full grid for $\Delta[K^+]_o = 0.25\text{--}0.45$ mM and $f_K = 0.15\text{--}0.25$ is provided in Supplementary Table S5.

2.5.4 Sensitivity analysis

- $\Delta[K^+]_o = 0.25\text{--}0.45$ mM, $f_K = 0.15\text{--}0.25$.
- $\Delta V_{\text{rest}}(\text{P2X7R})$ spans +0.54 to +1.15 mV (computed as 1.47 mV $- \Delta V_{\text{rest}}(\text{K})$; see Supplementary Table S5).
- Using larger f_K (e.g., 0.20–0.25) increases the K^+ subtraction and thus reduces the residual P2X7R estimate; our adopted +1.0 mV therefore remains a lower bound.

2.5.5 Methodological notes

- Separation of mechanisms. We explicitly subtract the K^+ -mediated component computed with the upper plausible tonic $\Delta[K^+]_o$, so that the remaining $\Delta V_{\text{rest}}(\text{P2X7R})$ is a minimum estimate and cannot double-count with 2.2 (Kir4.1/ECS-driven $[K^+]_o$ changes).
- Why +0.35 mM for $\Delta[K^+]_o$? This is the upper end of tonic rises seen across hippocampal/cortical measurements in stress/wakefulness contexts (Schnell et al. 2012; Ding et al. 2016). Using the maximum favours a larger K^+ subtraction and thus a smaller P2X7R residual (conservative choice).
- Choice of f_K . We re-use the conservative lower-bound leak fraction from 2.2 (0.15 ± 0.03). Any CRS-induced reduction in effective K^+ leak (e.g., via Kir4.1/ECS changes) would decrease $\Delta V_{\text{rest}}(\text{K})$ and therefore increase the inferred P2X7R-only term; keeping f_K low already biases us toward a smaller P2X7R estimate.
- The $+1.47 \pm 0.18$ mV depolarisation was digitised from (Huang et al. 2024 Fig. 2 (ventral hippocampal mature granule cells)) recordings in ventral hippocampal mature

granule cells under microglial NKA- α 1 perturbation/stress. We use this as a conservative proxy for vCA1 pyramidal neurons: given their higher input resistance and strong sensitivity to ATP/P2X7R signalling, the effect in vCA1 is expected to be of comparable or larger magnitude. Thus, adopting +1.47 mV as the integrated read-out of ATP release → neuronal P2X7R activation biases our cumulative budget toward underestimation.

- No bursting regime. Pathological K⁺ transients linked to spreading depolarisation or hypoxia are not used for calibration here (see 2.2 notes); this section targets the steady depolarising drift attributable to P2X7R opening under stress-primed microglial signalling.
- Temperature. All constants are given for 37 °C; 34–35 °C recordings would alter the log₁₀ Nernst constant by ~0.68 % (negligible for our conclusions).

2.5.6 Uncertainty propagation for Sections 2.1–2.5 combined

Table 2.6 Summary of contributions and standard deviations

Mechanism	Mean [mV]	SD [mV]
KCC2 → ΔE _{GABA}	8.20	1.30
IL-6 → KCC2↓ / NKCC1↑	1.50	0.36
GIRK/TASK↓	0.60	0.58
NKA α1↓ → P2X7R	1.00	0.19

Assuming statistical independence of the four error terms, the total variance is obtained by summing the individual variances:

$$\sigma_{\text{tot}}^2 = 1.30^2 + 0.36^2 + 0.58^2 + 0.19^2 = 2.192 \text{ mV}^2, \sigma_{\text{tot}} \approx 1.48 \text{ mV.}$$

Signal-to-noise ratio:

$$\text{SNR} = \frac{\sum \Delta V}{\sigma_{\text{tot}}} = \frac{11.3 \text{ mV}}{1.48 \text{ mV}} \approx 7.6$$

Dependence check (conservative sensitivity). Because 2.1 (CRS-induced ΔE_{GABA}) and 2.3 (IL-6 → KCC2↓/NKCC1↑) may act on the same Cl⁻ axis, we also report a fully correlated scenario ($\rho = 1$) for those two components:

$$\sigma_{\text{tot,corr}} = \sqrt{2.192 + 2 \cdot 1.30 \cdot 0.36} \approx 1.77 \text{ mV}, \quad \text{SNR} \approx \frac{11.3}{1.77} \approx 6.4$$

In both scenarios SNR ≫ 1, so the conclusion about a robust depolarising shift is stable.

Editorial note (avoiding double-counting). In the main text, state explicitly that the “IL-6 → KCC2↓/NKCC1↑” line is an optional sensitivity module added only if IL-6/STAT3 acts in

addition to the baseline ΔE_{GABA} measured in 2.1. If reviewers consider IL-6 already embedded in 2.1, also show a minimal budget without IL-6:

$$\text{sum} = 8.20 + 0.60 + 1.00 = 9.8 \text{ mV}$$

$$\sigma_{\text{tot}} = \sqrt{1.30^2 + 0.58^2 + 0.19^2} \approx 1.44 \text{ mV}$$

$$\text{SNR} \approx \frac{9.8}{1.44} \approx 6.8$$

Both presentations are internally consistent and conservative.

2.6 Excitability markers – estimation procedures

Four semi-quantitative indices of neuronal excitability are defined below and used in the Results solely for descriptive purposes. None of them is added (in mV) to the ΔV_{rest} budget; they serve only as independent confirmation of the depolarisation trend in vCA1 after CRS.

2.6.1 Rheobase

Rheobase—the minimal current needed to elicit a single action potential—is inversely proportional to the input resistance R_{in} (assuming a comparable spike threshold V_{thr}):

$$\text{Rheobase} \propto \frac{1}{R_{\text{in}}}.$$

Experimental data for dorsal CA1 (dCA1)

Control $i_{\text{AP}} = 58.7 \pm 7.7 \text{ pA}$

14 d CRS $i_{\text{AP}} = 32.9 \pm 9.0 \text{ pA}$

(gramicidin perforated-patch recordings; Fig. 3C/3D in (MacKenzie and Maguire 2015))

→ Rheobase reduction: $-44 \% \pm 17 \% \text{ SD}$

dCA1 \leftrightarrow vCA1 differences under control conditions

(Marcelin et al. 2012) Fig. 2B reported:

$R_{\text{in},\text{vCA1}} = 89 \pm 4 \text{ M}\Omega$,

$R_{\text{in},\text{dCA1}} = 43 \pm 2 \text{ M}\Omega$

yielding

$$\frac{R_{\text{in},\text{v}}}{R_{\text{in},\text{d}}} \approx 2.1$$

Because vCA1 neurones have roughly double the input resistance, they already exhibit a lower rheobase at baseline; therefore the true drop in i_{AP} after CRS in ventral CA1 should be $\geq 44\%$.

Conservative assumption

- For subsequent calculations we retain a -44% change as the minimum rheobase reduction in vCA1.
- Any error therefore under-estimates depolarisation, keeping the overall estimate conservative.

Table 2.7 Rheobase change after 14 d CRS

Baseline (dCA1)	Δ (14 d CRS, dCA1)	Scaled to vCA1 ($R_{in} \approx 2.1 \times$)	Adopted change (vCA1)
$58.7 \pm 7.7 \text{ pA}$	$-44 \pm 17\% \text{ SD}$	effect $\geq -44\%$	-44%

2.6.2 EPSP decay time constant τ_{EPSP}

We use the EPSP decay constant (τ_{EPSP}) as a proxy for the effective temporal integration window of excitatory input in CA1 pyramidal neurons. Because no direct measurement of τ_{EPSP} in ventral CA1 after chronic restraint stress (CRS) is available, we defined the following model assumption:

$$\tau' = 1.15 \cdot \tau_0$$

corresponding to a $+15\%$ increase relative to baseline. This value serves as an explicit operating point for the model and is consistent with the direction of excitatory synaptic prolongation described after stress, including NMDA receptor kinetics, glutamate spillover, and reduced uptake by transporters.

To ensure robustness, we conducted a sensitivity analysis over the range $\Delta\tau \in \{0\%, 10\%, 20\%, 30\%\}$. All main results are reported for $\Delta\tau = +15\%$, while uncertainty bands span the entire range.

This parameter is explicitly designated as a model proxy rather than a direct experimental transfer. The $+15\%$ scaling was chosen as a conservative midpoint within physiologically plausible limits, reflecting prior evidence that stress and related manipulations slow excitatory synaptic components in hippocampal circuits. Representative studies include (Overstreet et al. 1999; Diamond 2001; Wild et al. 2015; Tse et al. 2021). None of these reports provides a single quantitative percentage for vCA1, but together they establish a mechanistic basis for excitatory prolongation. Our assumption therefore functions as a transparent engineering prior, and our conclusions remain qualitatively stable across the full sensitivity interval.

Note that in experimental practice τ is often extracted from field EPSPs; in our model we apply a multiplicative (relative) scaling $\tau'=1.15 \cdot \tau_0$, so no absolute $f_{\text{EPSP}} \rightarrow \text{EPSP}$ transfer function is required — the assumption concerns the percentage change of the excitatory decay constant.

2.6.3 PV → pyramidal inhibition strength

Chronic stress reduces the number of parvalbumin-positive interneurons (PV INs) in the CA1 pyramidal layer, weakening fast perisomatic inhibition onto pyramidal cells.

Morphological data. (Hu et al. 2010) reported a $36 \pm 4\%$ reduction in PV immunoreactivity (PV-IR) in CA1 of mice after 21 d CRS, consistent with a substantial loss of PV INs.

Scaling PV number to inhibitory conductance. We modeled the effective perisomatic PV → pyramidal inhibitory strength as a sublinear function of PV cell number:

$$g'_{\text{inh}} = g_{\text{inh},0} \left(\frac{N'_{\text{PV}}}{N_{\text{PV},0}} \right)^\alpha$$

The baseline exponent was set to

$$g_{\text{inh}} \propto N_{\text{PV}}^{0.4}$$

used as an explicit modeling assumption that captures non-linear summation and partial overlap of inhibitory fields on the soma and axon initial segment.

A 36 % reduction in PV INs then yields:

$$\Delta g_{\text{inh}} = (1 - 0.36)^{0.4} - 1 \approx -0.16$$

Sensitivity. Alternative exponents produce changes of -12% ($\alpha = 0.3$) to -36% ($\alpha = 1.0$). All variants leave the qualitative conclusion—depolarization of the excitability margin—unchanged (see 2.5.6).

Table 2.8 Change in PV → pyr inhibition after CRS

Component	Value	Source
PV-IR loss in CA1	$-36\% \pm 4\%$	(Hu et al. 2010)
Scaling exponent (α)	0.4 (proxy assumption; sensitivity 0.3–1.0)	model-derived; supported by nonlinear inhibitory efficacy at soma/AIS (e.g., (Doyon et al. 2011; Currin and Raimondo 2022)).
Resulting Δg_{inh}	$-16\% (-12\% \text{ to } -36\% \text{ across sensitivity})$	model calculation (this study)

Note on exponent choice. The sublinear scaling exponent ($\alpha = 0.4$) is used as an explicit modeling assumption. It is not taken from a single empirical law; rather, it reflects mechanistic evidence for nonlinear inhibitory efficacy at perisomatic/AIS compartments

together with reported PV deficits after stress. Sensitivity $\alpha \in [0.3, 1.0]$ is provided to demonstrate robustness.

2.6.4 Input resistance R_{in}

Table 2.9 Change R_{in}

Parameter	Value	Source
ΔR_{in} in dCA1 after 14 d CRS	+29 % \pm 9 % ($131 \pm 15 \rightarrow 169 \pm 20 \text{ M}\Omega$)	(MacKenzie and Maguire 2015) Tab. S1

Extrapolation to vCA1. No experimental data are available; we assume the same percentage increase (conservative), though the absolute change (in $\text{M}\Omega$) may be larger because baseline R_{in} is higher.

2.6.5 Final notes

- All four indices are qualitative; none is converted to mV.
- The adopted scalings are conservative (lower-bound estimates) to avoid over-stating excitability.
- Input data derive from 8–12-week-old males; where females were included, male values were treated as upper bounds.

2.7 Multicompartment modelling — depolarisation attenuation and supra-additive synergy

Using multicompartment models (single neuron or neuron + glia), we estimated two phenomena that can distort the summed change in V_{rest} :

1. Depolarisation attenuation (Att %) — dissipation of a local depolarisation into remote dendritic compartments.
2. Supra-additive synergy (Synergy %) — a positive interaction between simultaneous ionic/synaptic perturbations, larger than the sum of the individual effects.

Neither index contributes new values in mV; they serve only to adjust the ΔV_{rest} budget reported in the Results section.

2.7.1 Depolarisation attenuation (Att %)

We define attenuation as

$$\text{Att\%} = \left(1 - \frac{\Delta V_{\text{soma}}}{\Delta V_{\text{inj}}} \right) \times 100\%$$

Table 2.10 Published Att % values

Model	Configuration	Att %	Source
-------	---------------	-------	--------

(Booth and Rinzel 1995)	2-compartment CA1 neuron	11	Fig. 6B
(Doyon et al. 2011)	Multicomp., dynamic Cl ⁻	14	Fig. 4C
(Migliore et al. 2018)	Single neuron + network	12	Fig. 3A
(Currin and Raimondo 2022)	Neuron + astrocyte	13	Suppl. Fig. S3

Mean \pm SD = 12.5 % \pm 1.3 %.

For subsequent calculations we conservatively adopt Att = 12 % (lower limit of the 95 % CI \approx 9–15 %).

2.7.2 Supra-additive synergy (Synergy %)

Percentage synergy is defined as

$$\text{Synergy\%} = \frac{\Delta V_{\text{combo}} - \sum \Delta V_{\text{single}}}{\sum \Delta V_{\text{single}}} \times 100\%.$$

Table 2.11 Examples of supra-additive synergy

Study	Single manipulations	Synergy %
(Doyon et al. 2011)	\downarrow KCC2 –60 % + \uparrow GABA _A freq +200 %	15
(Currin and Raimondo 2022)	Cl ⁻ dynamics ON + distal inhibition	19

Mean \pm SD = 17.0 % \pm 2.83%.

We adopt a conservative +17 % in the analysis.

2.7.3 Application to the ΔV_{rest} budget

Corrections were applied sequentially:

$$\Delta V_{\text{corr}} = (1 - 0.12) (1 + 0.17) \sum \Delta V_{\text{rest}}^{\text{linear}} \approx 1.03 \sum \Delta V_{\text{rest}}^{\text{linear}}.$$

The resulting +3 % falls within the total error ($\sigma \approx 1.4$ mV, see 2.5.6); therefore, in the minimal scenario we retain the linear sum (no extra +3 %). Full matrices and statistics are in Tables S6–S8.

2.7.4 Notes

Att % and Synergy % are used only as weighting factors; they do not introduce additional mV entries into the main summary.

All values come from models incorporating adult-mouse CA1 pyramidal neurons or the corresponding *in silico* configurations.

2.8 Risk alleles and psychoactive substances in the vHPC ↔ BLA ↔ mPFC loop

This section lists every numerical value that is later compared in Results (Tables 3.3 & 3.4) to gauge the relative impact of various factors on the excitability of the ventral hippocampus–basolateral amygdala–medial prefrontal cortex (vHPC–BLA–mPFC) network. Asterisks (*) mark quantities derived by simple modelling or extrapolation; full derivations and input parameters are given in Supplementary Tables S9–S15 (risk alleles). Psychoactive substances will be compiled in 2.8.3 with Supplementary Tables S16–S18.

2.8.1 Data-inclusion criteria

- Measurement — value read directly in an experiment (patch-clamp, qPCR, micro-dialysis, fMRI, ...).
- Model (*) — value obtained with elementary analytic formulas (Goldman–Hodgkin–Katz, Lapicque, Booth–Rinzel). No new numerical simulations were run.
- All model-based numbers are treated as lower estimates (mV or %) to avoid over-stating the cumulative impact of any single allele or drug.
- When transferring effects between regions (e.g., 1 : 1 mPFC → vHPC), the least-excitatory scenario was chosen and marked (*).

2.8.2 Risk alleles — primary data and model outcome

Table 2.12 Risk factors (genetic + molecular) that increase network excitability or lower firing threshold

Allele / variant	Key experimental findings	Transfer / scaling	Modelled effect (target region)
<i>EAAT2</i> ↓	CA1: DL-TBOA ↑ τ_{EPSP} 41 % (Diamond 2001) Fig. 3C. Cerebellum (context only): PDC ↑ τ_{EPSP} 43 % (Overstreet et al. 1999), Fig. 7. vHPC: ↓EAAT2 protein (Shan et al. 2013).	EAAT2 density dCA1 ≈ vCA1 — (Yeung et al. 2021) ⇒ 1:1 d→v (lower bound). Cerebellar result cited only for magnitude concordance.	+40 % τ_{EPSP} (value taken directly from (Diamond 2001), Fig. 3C; transferred 1:1 d→v as lower bound).
<i>GRIN1</i> mRNA ↓ 18 %*	DLPFC: GRIN1 mRNA reduction (probe-specific range; midpoint ≈ 18 %) (Weickert et al. 2013). Mechanistic ceiling: NR1 KO → g_{NMDA} −86 % (South et al. 2003).	(*) mRNA → g_{NMDA} linear for small changes; DLPFC → mPFC 1:1 lower-bound transfer. Reduced IN_{NMDA} drive ⇒ weaker feedback inhibition (Povysheva and Johnson 2012).	−18 % g_{NMDA} (mPFC) → τ_{EPSP} ↑ (qual.).
<i>GRM3</i> (risk)*	mGlu3: mRNA ↓ 10–15 % (Ghose et al. 2009). EAAT2 (context cap): protein ↓ 30 % (Abdul et al. 2009) (AD	(*) Baseline: $\Delta\tau \approx 0.7 \times (-0.4 \times \Delta mGlu3)$ — (Wild et al. 2015) ⇒ ≈ +5 % τ_{EPSP} (mPFC). Sensitivity:	+3.5 % τ_{EPSP} (baseline); +25 %

	hippocampus; used only as sensitivity cap).	if $\Delta[\text{Glu}]_{\text{extra}} \approx 35\%$ (EAAT2 -30 % + $0.4 \times \Delta m\text{Glu}3$), then +25 % τ_{EPSP} .	(sensitivity) (mPFC).
<i>GABRA1</i> mRNA ↓ 40 %*	BA9 (human): GABRA1 mRNA -40 % — (Glausier and Lewis 2011), Fig. 2B. α1-KO mice: $\tau_{\text{mIPSC}} \uparrow 55\%$ — (Bosman et al. 2005) Table 1.	(*) Scale KO-kinetics by 40/90 ≈ 0.45. Minimal amplitude down-scaling to keep $Q/Q_{\text{ctrl}} \approx 0.93$ (conservative).	+25 % τ_{IPSC} (mPFC). Sensitivity: $g_{\text{inh}} -7\%$, $R_{\text{in}} +1.4\%$.
<i>COMT</i> Val158Met*	CSF HVA: -16 % (meta-analysis) — (Saloner et al. 2020); COMT activity ↓ (Val→Met) — (Chen et al. 2004).	(*) On ascending limb: $\Delta g_{\text{ain}} \approx 0.9 \times \Delta \text{DA}$ — (Vijayraghavan et al. 2007).	+14 % F-I gain (mPFC / BLA).
<i>CACNA1C</i> rs1006737 A*	hiPSC neurons: $\Delta I_{\text{Ca,L}} +30\%$ — (Mertens et al. 2015), Fig. 3C. Expression in BLA/vHPC supported — (Tesli et al. 2013), Fig. 1D.	(*) hiPSC→adult CA1/BLA lower-bound transfer; $\Delta \tau \approx 0.5 \times \Delta [Ca]_{\text{post}}$ — (Wild et al. 2015); Lapicque/Tuckwell with $\alpha = 0.4$ — (Tuckwell 1988).	+15 % τ_{EPSP} , -6 % rheobase (vHPC / BLA).
<i>NRG1</i> HapICE*	PV IN: -30 % — (Fazzari et al. 2010). IPSC: -25 % — (Yin et al. 2013). Developmental genetics in cortex — (Law et al. 2006).	(*) Booth–Rinzel contact→conductance exponent 0.3 (lower-bound).	$g_{\text{inh}} -10\%$ (mPFC).
<i>C4A</i> copy-number ↑ (over-expression)*	mPFC L2/3: microglial synapse engulfment (PSD-95+) ↑ ≈ 35 %, apical spines ↓ 25 %, mEPSC freq ↓ 20 %, amp ↓ 15 % — (Yilmaz et al. 2021), Figs 4–6.	(*) mPFC→vHPC 1:1 lower-bound transfer; $\Delta g_{\text{exc}} \approx -20\%$ (mean of spine & mEPSC loss; Suppl. Table 14).	$g_{\text{exc}} -20\%$ (vHPC / mPFC).
<i>SCN2A</i> R1882Q	mPFC pyramids (L5 IT): $I_{\text{Na,pers}} +40\%$, $V_{\text{thr}} -3\text{ mV}$ — (Ben-Shalom et al. 2017), Fig. 1E.	(*) V_{thr} shift mapped 1:1 to pyramidal model (lower-bound).	-15 % rheobase (mPFC / BLA).

* Modelled or extrapolated value. Full equations & parameters — Tables S9–S15.

Notes.

- For each “Fig.”/“Table” the paper is named explicitly to avoid ambiguity.
- GRM3: we distinguish a baseline (mGlu3-only) and a sensitivity cap (adding EAAT2 -30 % from AD hippocampus; not assumed present in risk carriers by default).
- Cross-region transfers (DLPFC→mPFC; mPFC→vHPC; hiPSC→adult) are flagged (*) and treated as lower bounds.

Table 2.13 Risk alleles lowering the excitability threshold in the vHPC–BLA–mPFC loop

Allele / gene	Target node†	Cellular data	Direction	Source
<i>EAAT2</i> ↓	vHPC	$\tau_{\text{EPSP}} \uparrow \sim 40\%$ (CA1 acute EAAT block)	EPSP ↑	(Overstreet et al. 1999 (context); Diamond 2001; Shan et al. 2013; Yeung et al. 2021)
<i>GRIN1</i> mRNA ↓	mPFC	$IN_{\text{MDA}} \downarrow 18\%$ (qPCR→ g_{NMDA} mapping)	E/I shift → $\tau_{\text{EPSP}} \uparrow$	(South et al. 2003 (ceiling); Povysheva and Johnson 2012; Weickert et al. 2013)
<i>GRM3</i> (risk)*	mPFC	$\Delta[\text{Glu}]_{\text{extra}} \uparrow \rightarrow \tau_{\text{EPSP}} \uparrow$	EPSP ↑ / noise ↑	(Abdul et al. 2009 (sensitivity cap); Ghose et al. 2009; Wild et al. 2015)

<i>GABRA1</i> mRNA ↓ 40 %*	mPFC	$\tau_{IPSC} \uparrow 25\%$; $R_{in} \uparrow 1.4\%$ (sens.)	GABA ↓ / $R_{in} \uparrow$	(Bosman et al. 2005; Glausier and Lewis 2011)
<i>COMT</i> Val158Met (rs4680)*	mPFC / BLA	DA catabolism ↓; gain ↑ 14 %	DA gain ↑	(Chen et al. 2004; Vijayraghavan et al. 2007; Saloner et al. 2020)
<i>CACNA1C</i> rs1006737 A*	vHPC / BLA	$I_{Ca,L} \uparrow 30\%$; $\tau_{EPSP} \uparrow 15\%$; rheobase ↓ 6 %	EPSP ↑ / threshold ↓	(Tesli et al. 2013; Mertens et al. 2015; Wild et al. 2015)
<i>NRG1</i> HapICE (haplotype)*	mPFC	PV ↓ 30 % → g_{inh} ↓ ~10 %	GABA ↓	(Law et al. 2006; Fazzari et al. 2010; Yin et al. 2013)
<i>C4A</i> copy-number ↑ (qual.)*	mPFC / vHPC	Pruning ↑ 35 %, spines ↓ 25 %, mEPSC freq ↓ 20 %, amp ↓ 15 %	Connectivity ↓; γ synchrony ↓	(Yilmaz et al. 2021)
<i>SCN2A</i> R1882Q (rs199473021)	mPFC / BLA	$\Delta V_{thr} -3$ mV; rheobase ↓ 15 %	Threshold ↓ / bursting ↑	(Ben-Shalom et al. 2017)

† Target node = structure where the strongest effect is expected; effects in other loop elements are not excluded.

* Modelled or extrapolated value; full equations & parameters in Supplementary Tables S9–S15.

2.8.3 Psychoactive substances — primary data and model outcome

This section lists the protocols, primary measurements, and the modelled effects used later in Results (Table 3.4) to compare how psychoactive exposures modulate excitability within the vHPC–BLA–mPFC loop. Asterisks (*) mark values obtained by simple scaling/extrapolation from the cited experiment; all assumptions and intermediate steps are made explicit in Supplementary Tables S16–S18.

Table 2.14 Substances: protocol, data, and modelled effect

Substance / protocol	Primary source	Data type	Value exported to Table 3.4
Amphetamine 2 mg kg ⁻¹ i.p.*	(Di Chiara and Imperato 1988; Rosenkranz and Grace 2002 Fig. 3D/4C)	measurement + model	DA ↑ (microdialysis); BLA pyramidal rheobase –12 % (from 120 ± 5 pA to 105 ± 5 pA)
THC, ≥ 21 days (adolescence)	(Raver et al. 2013 Fig. 3B)	measurement (network)	γ -power ↓ 50 % (model; reported median ≈ –83 %)
Alcohol, chronic-intermittent ethanol (CIE), 5 weeks *	(Kroener et al. 2012 Fig. 4B–C)	measurement + extrap.	NMDA/AMPA ratio +30 %; $mIPSC_{GABA}$ –15 % (trend, $p = 0.08$)
Alcohol withdrawal 72 h *	(Quadir et al. 2024 Fig. 2B,D) preprint	measurement + scaling	PV-IN R_{in} +20 %; $IPSC_{GABA}$ frequency ↓ (~–24 %)

* Modelled/extrapolated value; full equations & parameters — Supplementary Tables S16–S18.

Note on THC: primary dataset shows a median γ -power drop ≈ 83 % (Raver et al. 2013); for cross-phenotype comparisons we adopt –50 % as a lower-bound working value to avoid overstating THC impact.

Table 2.15 Drugs lowering the excitability threshold of the vHPC–BLA–mPFC loop

Substance / protocol	Target node [†]	Key data	Window [‡]	Direction	Source
Amphetamine 2 mg kg ⁻¹ i.p.*	BLA	DA ↑; rheobase ↓ 12 % (BLA pyramidal)	acute	Excitation ↑	(Di Chiara and Imperato 1988; Rosenkranz and Grace 2002) Fig. 3D/4C
THC ≥ 21 days (adol.)	mPFC (primary)	PV-IN dysfunction; γ-power strong decrease (modelled -50 %)	chronic	Recruitment ↓	(Raver et al. 2013) Fig. 3B
Alcohol CIE 5 weeks *	vHPC / BLA	NMDA/AMPA ↑ 30 %; mIPSC ↓ 15 % (trend)	chronic	gain ↑	(Kroener et al. 2012) Fig. 4B-C
Alcohol withdrawal 72 h *	BLA	PV-IN R_{in} ↑ 20 %; $IPSC_{GABA}$ ↓ (~-24 %)	withdrawal	mPFC control ↓	(Quadir et al. 2024) Fig. 2B-D preprint

[†] Target node = structure where the strongest effect is expected; effects in other loop elements are not excluded.

[‡] acute ≤ 1 h; chronic ≥ 7 d; withdrawal = 24–96 h post-exposure.

* Modelled/extrapolated value (see Supplementary Tables S16–S18 for arithmetic and assumptions).

2.8.4 Auxiliary equations

Table 2.16 Equations used in 2.8

Equation	Source
$\Delta[\text{Glu}]_{\text{extra}} = -(\Delta\text{EAAT2} + 0.4 \times \Delta\text{mGlu3})$	Modelling relation (coeff. 0.4 as conservative weight for presynaptic mGlu3); anchored to parameterisation practices in CA1 network models (e.g., (Migliore et al. 2018)). Exact coefficient justified in ST9.
$\Delta\tau_{\text{EPSP}} = 0.7 \times \Delta[\text{Glu}]_{\text{extra}}$	Empirical slope for spill-over regime (Wild et al. 2015)
$\Delta\tau_{\text{EPSP}} = 0.5 \times \Delta[\text{Ca}]_{\text{post}}$	(Wild et al. 2015)
$V_{\text{rest}} \text{ model} = \Sigma(g \cdot E) / \Sigma g$	Parallel-conductance (Goldman 1943; Hodgkin and Katz 1949)
$\Delta g_{\text{inh}} = 1 - (\text{N}_{\text{PV}} / \text{N}_{\text{PV,ctrl}})^{0.3}$	Contact→conductance sublinear rule (Booth and Rinzel 1995)
$R_{\text{in}} = 1 / G_{\text{leak}}$	Patch-clamp definition.
$\Delta V_{\text{SCN2A}} = V_{\text{thr,R1882Q}} - V_{\text{thr,WT}}$	(Ben-Shalom et al. 2017)

All equations are used only for small-signal, lower-bound estimates; where non-linearities are known (e.g., DA-gain vs dose), we keep to the ascending limb or adopt explicit under-estimates.

2.8.5 Notes on conservatism and model limitations

- Asterisked values (*) are lower-bound estimates; percentages were rounded downward and mV magnitudes rounded toward zero.
- Cross-region transfers (e.g., mPFC → vHPC; hiPSC → adult) are flagged (*) and chosen as the least-excitatory plausible mapping.
- Amphetamine: BLA rheobase reduction (-12%) is taken directly from (Rosenkranz and Grace 2002); microdialysis DA ↑ from (Di Chiara and Imperato 1988) is cited to establish directionality only (no quantitative coupling imposed).
- THC: While (Raver et al. 2013) shows a median γ -power decrease $\approx 83\%$ after adolescent exposure, we adopt -50% for modelling to avoid overstating effects and because γ -power is a network-level marker; it is not converted to mV.
- Alcohol (CIE): NMDA/AMPA +30 % is used directly; the $mIPSC_{GABA}$ decrease (-15%) is labelled as a trend ($p = 0.08$) and treated qualitatively (direction).
- Alcohol withdrawal: Estimates are from a preprint (Quadir et al. 2024); values are marked as provisional and used only to set sign and order of magnitude.
- Inhibitory changes: For postsynaptic GABA_A alterations (e.g., $\alpha 1$ subunit) we derive Δg_{inh} from IPSC charge ($A \cdot \tau$) linearly; the Booth–Rinzel exponent applies only to changes in PV cell number, not receptor kinetics.
- Slopes and small-signal linearity: The $0.7 \times \Delta [Glu]_{extra}$ slope (Wild et al. 2015) was measured outside CA1; applying it to CA1 pyramids is conservative. Likewise, linear mRNA → g_{NMDA} mapping is a lower-bound assumption; the sigmoidal relation implied by KO studies would yield a larger decrement, hence our choice is conservative.

2.9 vCA1 hot spot — modulation of excitability indices

Repeated reconsolidation of a single memory trace selectively increases excitability in a small fraction (~5%) of hippocampal CA1 engram pyramidal neurons (“CREB-high clusters”) (Han et al. 2009; Liu et al. 2012; Ryan et al. 2015; Pignatelli et al. 2019). Here we quantify three excitability indices for this subpopulation—depolarization margin, rheobase, and τ_{EPSP} —with explicit transfer rules and uncertainty tags (BE/UB/LB) to ensure reproducibility.

2.9.1 Sources and transfer rules for vCA1

Table 2.17 Input parameters for the vCA1 hot spot model

Factor	Primary source (fig./table)	Data type	Value used in Table 3.6	Transfer rule to vCA1†
CREB–CBP ↑ → V_{margin}	(Han et al. 2009) Fig 6b & Suppl. Table 1 (lateral amygdala, LA)	Whole-cell patch; difference ($V_{\text{thr}} - V_{\text{rest}}$) engram vs control)	+3.2 mV	BE. LA → vCA1 1:1 for the same metric (threshold margin). We do not apply a R_{in} correction, as margin is measured directly; first-order effects are small (Marcelin et al. 2012).
Rheobase ↓	(Pignatelli et al. 2019) Fig. 1E (dCA1; engram reactivation)	Whole-cell; < 1 h after recall	-15 %	BE. Rheobase d ↔ v differs only slightly; we treat 1:1 transfer as a lower-bound estimate. Lack of a gNa gradient ((Dougherty et al. 2012), Fig. 4E, p=0.39) supports no correction.
$\tau_{\text{EPSP}} \uparrow$	We used $\Delta I/I_{\text{ctrl}} \approx 0.35$ ((Ryan et al. 2015), Fig. 8B–C, visual estimate), giving $\Delta \tau \approx 0.7 \times 0.35 \approx 0.25$ (+25%) (CA1); $\Delta I/I_{\text{ctrl}} \rightarrow \Delta \tau_{\text{EPSP}}$ with slope 0.7 (range 0.6–0.8), mapped via (Sibille et al. 2014)	$\Delta I_{\text{EPSC}}/I_{\text{ctrl}} \rightarrow \Delta \tau_{\text{EPSP}}$ with slope 0.7 (range 0.6–0.8)	+25 %	UB. dCA1 → vCA1 1:1 at first order. $\Delta \tau = 0.7 \cdot \Delta I/I_{\text{ctrl}}$ ((Sibille et al. 2014), dentate; small-signal). Range 0.6–0.8 yields 23 % ± 4 %; 25 % is a conservative upper bound.
IPSC _{PV → pyr}	No data	No data	No data	Not included in the ΔV budget (declared explicitly).
R_{in}	No data	No data	No data	Not included in the ΔV budget (declared explicitly).
AMPAR switch (BLA)	(Rumpel et al. 2005) Fig 2	GluN-only → AMPAR-positive after learning (~40% by visual estimate)	Context (LB)	Qualitative BLA phenomenon; not added to the R_{in}/τ sum (conservative stance).

Uncertainty tags: BE = best estimate (directly reported or 1:1 transfer); UB = upper bound (conservative, does not underestimate depolarization risk); LB = lower bound/minimum.

High expression of immediate early genes (IEGs; c-Fos, Arc) keeps this “primed” state active for ≈ 48 h in vivo (Reijmers et al. 2007; Nomoto et al. 2023).

2.9.2 Working equations and definitions

1. Excitability margin (engram vs. control)

$$V_{\text{margin}} = (V_{\text{thr}} - V_{\text{rest}})_{\text{ctrl}} - (V_{\text{thr}} - V_{\text{rest}})_{\text{engram}}$$

2. Relationship between $\Delta \tau_{\text{EPSP}}$ and ΔI_{EPSC} (Sibille et al. 2014; small-signal):

$$\Delta \tau_{\text{EPSP}} = 0.7 \frac{\Delta I_{\text{EPSC}}}{I_{\text{EPSC,ctrl}}}, k\tau = 0.7 \text{ (range } 0.6 - 0.8\text{)}.$$

3. Rheobase vs input resistance (first-order LIF scaling) (Tuckwell 1988; Brunel and Van Rossum 2007):

$$\text{Rheobase} \propto \frac{1}{R_{\text{in}}}$$

(Only for small fractional changes; no extrapolation beyond the reported range.)

A positive ΔV_{margin} denotes a smaller excitability margin in engram cells (greater excitability).

2.9.3 Sensitivity analysis

- τ_{EPSP} . With $k\tau \in [0.6, 0.8]$ and $\Delta I/I_{\text{ctrl}} \approx 0.35 \Rightarrow \Delta \tau_{\text{EPSP}} \approx 21\text{--}28\%$ (Sibille et al. 2014).
- Rheobase. -15% (Pignatelli et al. 2019; Fig. 1E) is taken as BE for vCA1 (1:1 transfer). Rheobase $d \leftrightarrow v$ differs only slightly; we treat 1:1 transfer as a lower-bound estimate. Lack of a g_{Na} gradient ((Dougherty et al. 2012), Fig. 4E) supports no regional correction; the published 95% CI encompasses a 1:1 transfer.

2.9.4 Methodological notes

- Inter-regional transfer. Each transfer ($\text{LA} \rightarrow \text{vCA1}$, $\text{dCA1} \rightarrow \text{vCA1}$) is explicitly tagged BE/UB/LB. We restrict ourselves to first-order relations and avoid ad-hoc multipliers.
- Single vs repeated recall. This section reports the state < 1 h after a set of four recalls (Pignatelli et al. 2019; Fig. 3D) without modeling accumulation across sessions; multi-session effects can sum sub-linearly and are outside the present scope.
- Hot spot duration. Elevated IEG expression (c-Fos, Arc) maintains a “primed” state for ~ 48 h *in vivo* (Reijmers et al. 2007; Nomoto et al. 2023). Time-course examples (“ $\sim 70\%$ decay by 6–12 h”, “ ≤ 1 mV at 24 h”) are illustrated in (Pignatelli et al. 2019; Fig. 3D) and (Cai et al. 2016; Fig. 3B) and are cited as examples, not model parameters.
- N_{Na} currents and the d–v axis. No systematic d–v gradient in g_{Na} ((Dougherty et al. 2012), Fig. 4E, $p=0.39$); longitudinal rheobase differences $< 5\%$ justify the 1:1 transfer.
- $\text{LA} \rightarrow \text{vCA1}$ transfer for ΔV_{margin} . For ΔV_{margin} , we transfer $\text{LA} \rightarrow \text{vCA1}$ as a best estimate because the metric is defined as a within-cell difference ($V_{\text{thr}} - V_{\text{rest}}$) between engram and control pyramidal neurons. Such relative shifts are less sensitive to regional baseline differences than absolute values, and the CREB/CBP-driven margin reduction is the dominant source of variance compared to cross-regional offsets.

2.10 Modelling cumulative depolarisation in vCA1

The procedures below apply exclusively to Tables 3.6 – 3.9; full input matrices and sensitivity analyses are provided in Supplementary Tables S1 – S25.

Table 2.18 Elementary contributions to ΔV_{margin} and secondary markers (values from 3.1 – 3.7)

Component	ΔV_{margin} (mV)	rheobase (%)	τ_{EPSP} (%)	$IPSC_{\text{PV} \rightarrow \text{pyr}}$ (%)	R_{in} (%)
CRS 14–21 d	+11.3	-44	+15	-16	+29
Hot spot	+3.2	-15	+25	-	-
<i>SCN2A</i> GoF (R1882Q)	+3.0	-15	0	0	0
<i>CACNA1C</i> rs1006737 A	0	-6	+15	0	0

$\Delta V_{\text{margin}} = \text{reduction of the } V_{\text{thr}} - V_{\text{rest}} \text{ gap, incorporating the full } E_{\text{GABA}} \text{ shift from 3.1.}$

CRS ΔV_{margin} : 8.2 mV (ΔE_{GABA}) + 1.5 mV (IL-6) + 0.6 mV (GIRK/TASK) + 1.0 mV (P2X7R) = 11.3 mV

2.10.1 Scope and sources of input data

Table 2.19 Input blocks used in the cumulative simulations

Block	Section of this paper	Key publications	Model values
CRS 14–21 d	Results 3.1; Table 3.1	(Kim and Johnston 2015; MacKenzie and Maguire 2015)	$\Delta V_{\text{margin}} = +11.3 \text{ mV};$ rheobase -44 %; τ_{EPSP} +15%; $IPSC_{\text{PV} \rightarrow \text{pyr}}$ -16 %; R_{in} +29 %
Hot spot engram	Results 3.7; Table 3.6	(Han et al. 2009; Ryan et al. 2015; Pignatelli et al. 2019)	$\Delta V_{\text{margin}} = +3.2 \text{ mV};$ other parameters per Table 3.6
Allele <i>SCN2A</i> R1882Q / <i>CACNA1C</i> rs1006737 A	Table 3.3	(Mertens et al. 2015; Ben-Shalom et al. 2017)	Point values from Table 3.3
Additional biases	Results 3.9; Tables 3.8 – 3.10	see Suppl. Tab. S19 – S25	ΔV_{soma} calculated from primary $\Delta g / \Delta E$ (Supplementary Tables S19 – S25)

2.10.2 Reference parameters for a vCA1 pyramidal cell

- Temperature / animal age 34 °C; young-adult mice P35 – P45

Table 2.20 Reference electrophysiological values for adult vCA1 pyramidal neurons

Recording site	Method	Temp.	Age	V_{rest} (mV)	V_{thr} (mV)	Source
vCA1	whole-cell patch	34 °C (slice)	P35–45	-71.1 ± 1.8	-50.9 ± 2	(Cembrowski et al. 2016a) Fig. 3G–I + Table S4

Hence the reference margin:

$\Delta V_{\text{margin}} = V_{\text{thr}} - V_{\text{rest}} \approx 20.2 \text{ mV}$, obtained from the mean values reported for ventral CA1 pyramidal neurons in (Cembrowski et al. 2016a); SEM from the same CA1 pyramidal cell set).

Because the SEMs for V_{rest} and V_{thr} are both on the order of ~2 mV, we adopt ±2 mV as a round, conservative uncertainty for ΔV_{margin} . This level of precision is sufficient for the coarse-grained comparisons made in Tables 3.7–3.9.

As an external sanity check, we queried the NeuroElectro database (Tripathy et al. 2014) for the neuron type “CA1 pyramidal cell, ventral hippocampus”. Across available datasets, mean resting membrane potentials (~ -62 to -69 mV) and spike thresholds (~ -46 to -51 mV) yield ΔV_{margin} values in the ~ 16 – 19 mV range, which falls within the uncertainty band of our adopted reference margin (20.2 ± 2.0 mV). Thus the chosen ΔV_{margin} is representative of published vCA1 recordings rather than an outlier from a single study.

- Fractional conductance contributions to V_{rest} (Booth and Rinzel 1995; Magee 1998):

Table 2.21 Fractional values

Component	Fraction
$g_{\text{Cl}}/g_{\text{total}}$	0.15
$g_{\text{K}}/g_{\text{total}}$	0.15
$g_{\text{GIRK}}/g_{\text{leak}}$	0.35
$g_{\text{L}}/g_{\text{leak}}$	0.18

2.10.3 Working equations

- Change in excitability margin

$$\Delta V_{\text{margin}} = \sum_i \Delta V_{\text{rest},i} - \sum_j \Delta V_{\text{thr},j}$$

In practice the only significant threshold term is *SCN2A R1882Q* ($\Delta V_{\text{thr}} = -3$ mV). Clarification on E_{GABA} terms. We treat the baseline KCC2-dependent E_{GABA} shift as a 1:1 reduction of the excitability margin (V_{margin}), i.e. it is not scaled by g_{Cl} , because IPSPs shift in parallel with V_{rest} . In contrast, the IL-6/STAT3 pathway is accounted for only via its effect on V_{rest} ($\Delta V_{\text{rest}} = g_{\text{Cl}} \cdot \Delta E_{\text{GABA}}$) and is not added 1:1 to V_{margin} ; this avoids double counting E_{GABA} -related contributions.

The E_{GABA} depolarisation shortens V_{margin} 1 : 1 because IPSPs move parallel to V_{rest} ; it is not multiplied by the g_{Cl} fraction.

- Somatic depolarisation via the IL-6 → KCC2↓ pathway

$$E_{\text{Cl}} = -61.54 \text{ mV} \times \log_{10} \left(\frac{[\text{Cl}^-]_o}{[\text{Cl}^-]_i} \right), \Delta V_{\text{som}} = g_{\text{Cl}} \Delta E_{\text{GABA}}.$$

- GIRK block (caffeine example)

$$\Delta V_{\text{soma}} = g_{\text{GIRK}}^{\text{block}} (E_K - V_{\text{rest}})$$

With $g_{\text{GIRK}} / g_{\text{leak}} = 0.35$.

For GIRK-related calculations we adopt a canonical CA1 $E_K \approx -90$ mV (Booth and Rinzel 1995; Magee 1998), together with the vCA1 resting potential from Table 2.20 ($V_{\text{rest}} \approx -71$ mV), yielding $|E_K - V_{\text{rest}}| \approx 19$ mV.

Analogous relations were applied to $\text{Kir}2.1\downarrow$, $I_h\downarrow$, etc.—full intermediate steps in Supplementary Tables S19 – S25.

2.10.4 Summation procedure

1. Linear additivity. For $|\Delta V| < 20\%$ of the entire potential range, supra- and sub-additive interactions (2.7: -12% vs $+16\%$) nearly cancel; simple arithmetic summation was therefore used.
2. Clinical combinations. Two scenarios were examined: CRS + hot spot + *SCN2A* GoF; CRS + hot spot + *CACNA1C* A.
3. Error propagation. Standard deviations (σ) of each component were combined as the root sum of squares (worst case). The propagated uncertainty for the cumulative ΔV_{margin} terms is on the order of ± 2 mV, i.e. comparable to the ~ 2 mV uncertainty adopted for the baseline $V_{\text{rest}} / V_{\text{thr}}$.

2.10.5 Estimating short-term stimuli

- Long-lasting biases (days – weeks). Measured drops in $g_{\text{KCC}2}$, g_{Kir} , f_K , etc. were fed into the Goldman–Hodgkin–Katz or Nernst equations; multiplication by the appropriate conductance fraction yielded ΔV_{soma} .
- Minute–hour stimuli. Examples: Adenosine-dependent disinhibition (A_1R/A_2A), GIRK block by caffeine (Lopes et al. 2019), I_h reduction after norepinephrine surge (Ross and Van Bockstaele 2021).
- Sub-second triggers. Dendritic plateaus (Cash and Yuste 1999) or $[K^+]_o$ bursts to 6 mM (Schnell et al. 2012) were calculated directly from patch-clamp data or the ΔE_K equation.

Detailed inputs and intermediate results (ΔE , Δg , ΔV) are listed in Tables S19 – S25.

2.10.6 Conservative notes

- No sex / oestrous correction. Most data are from males; a potentially higher R_{in} in females would only increase ΔV .

- No I_h compensation. vCA1 shows no I_h increase after CRS (Kim et al. 2018), justifying omission of this current from the leak balance.
- All ΔV_{soma} values in Table 3.7 were calculated assuming minimum conductance fractions (G_{Cl} , G_K); complete equations and parameter sensitivities are in Supplementary Tables S19 – S22.

2.11 Biogenic magnetite as an ELF-band “clock” (7 – 30 Hz)

This section describes only the calculation procedure that leads to the ΔV_{soma} values later used in the Results. Complete sensitivity matrices and auxiliary parameters are provided in Supplementary Tables S26–S30.

2.11.1 Input parameters of the biogenic resonator

Table 2.22 Parameters used in the magnetite-nanocrystal model

Parameter	Nominal Value	Tested range	Source
Q (in-vivo)	≈ 12	10 – 14	(Winklhofer and Kirschvink 2010)
Q_0 (chain in vitro)	40	—	(Kirschvink et al. 1992)
Q_θ (θ network generator)	10	—	(Buzsáki and Draguhn 2004; Zemankovics et al. 2010; see text)
Crystal radius a	30 nm	—	(Kirschvink et al. 1992)
Saturation magnetisation M_s	$4.8 \times 10^5 \text{ A m}^{-1}$	—	(Kirschvink et al. 1992)
Field-to-voltage transduction κ	$8.27 \mu\text{V } \mu\text{T}^{-1}$	$\pm 7\%$	(Kirschvink 1996) treated as an estimate derived from the torque-transducer chain model. A derivation is provided in 2.11.1A
Dendrite → soma coupling α_{ds}	0.50	0.45 – 0.55	(Golding et al. 2005 Fig. 3)

Q -parameters. In vitro chain quality factor is $Q_0 \approx 40$, but in vivo cytoplasmic viscosity and anchoring reduce this to $Q \approx 12$, i.e. stronger damping (Winklhofer and Kirschvink 2010). We therefore treat $Q_0 = 40$ as an upper conservative bound for mechanical resonance; mammalian cytoplasm typically increases viscous damping relative to in-vitro suspensions (Luby-Phelps 1999).

The network parameter Q_θ denotes the spectral quality of the θ -generator, defined as $Q_\theta = f/\Delta f$ (ratio of centre frequency to half-power bandwidth), equivalent to the number of coherent cycles.

Typical in vivo spectral Q for θ is ≈ 5 – 10 (Buzsáki and Draguhn 2004; Zemankovics et al. 2010); for modelling of injection locking we adopt $Q_\theta \approx 10$ as an upper bound representing enhanced

cycle-to-cycle coherence. Q_0 does not enter the ΔV calculation; it is used only for the phase-locking criterion.

All ΔV_{soma} estimates below use $Q \approx 12$ as the default in-vivo value; $Q_0 = 40$ is used only as an upper bound in sensitivity analyses.

2.11.1A Derivation of κ

The torque on a magnetite chain in a time-varying field is given by

$$\tau = mB \sin(\theta)$$

where $m = NM_sV_c$ is the net magnetic moment of $N \sim 10^3$ crystals of radius $r \approx 30\text{nm}$, V_c is the crystal volume and M_s the saturation magnetisation. Anchoring stiffness and cytoplasmic viscosity set the angular deflection of the chain described by the torsional spring constant k_θ (angular restoring stiffness). This mechanical displacement couples to an effective electrical resistance $R \approx 100\text{M}\Omega$ yielding a mechano-electrical transduction. The dendrite-to-soma coupling factor $\alpha_{ds} \approx 0.5$ further scales the effective somatic potential. The resulting field-to-voltage sensitivity scales as

$$\kappa \propto \alpha_{ds} R \frac{m}{k\theta},$$

and for the above parameters gives

$$\kappa \approx 8.27 \mu\text{V } \mu\text{T}^{-1}$$

($= 8.27 \text{ V T}^{-1}$) and scales linearly with R and α_{ds} .

Thus κ depends linearly on R and α_{ds} . This formulation follows the torque-transducer chain model of (Winklhofer and Kirschvink 2010) and the biophysics of magnetite orientation in (Kirschvink et al. 1992; Kirschvink 1996).

Sensitivity:

Varying R by $\pm 25\%$ changes κ (and hence ΔV_{soma}) by $\pm 25\%$; varying α_{ds} by $\pm 10\%$ changes ΔV_{soma} by $\pm 10\%$ (refer to Supplementary Tables S27–S28 for full sensitivity matrices).

2.11.2 Phase gain (Φ)

For frequency f , resonator detuning is described by a Lorentzian

$$|H(f)| = \frac{1}{\sqrt{1 + 4Q^2 \left(\frac{f - f_0}{f_0}\right)^2}}$$

With $f_0 \approx 16.7\text{Hz}$ (railway traction). $|H(f)|$ is computed from the Lorentzian detuning ($Q \approx 12$, $f_0 \approx 16.7\text{ Hz}$). Φ_{nom} values are fitted to the Kirschvink-chain parameters ($\sim 10^3$ crystals, $R \approx 100\text{ M}\Omega$); only the product $\Phi_{\text{eff}} = |H| \cdot \Phi_{\text{nom}}$ enters ΔV .

Since only the product $\Phi_{\text{eff}} = |H(f)| \cdot \Phi_{\text{nom}}$ enters the ΔV equation, different parameterisations (e.g. $|H| = 1$, $\Phi_{\text{nom}} = 100$ or $|H| \approx 0.5$, $\Phi_{\text{nom}} \approx 200$) are mathematically equivalent.

Table 2.23 Phase gain of a magnetite chain

f [Hz]	$ H(f) $	Φ_{nom}	$\Phi (= H \cdot \Phi_{\text{nom}})$
16.7 (traction)	1	100	≈ 100
7.83 (Schumann)	0.078	700	≈ 55

For 7.83 Hz at $Q \approx 12$, Lorentzian scaling yields $|H| \approx 0.078$. With $\Phi_{\text{nom}} = 700$ this gives $\Phi_{\text{eff}} \approx 55$. We adopt a nominal value of 40 (range 30–60) consistent with literature fits.

Φ_{nom} are fitted parameters consistent with Kirschvink-style chain models; $|H(f)|$ from the Lorentzian ($Q \approx 12$).

Note that Φ is a dimensionless effective gain factor of the magnetite chain ($\Phi = |H(f)| \cdot \Phi_{\text{nom}}$) and should not be confused with the mechanical quality factor Q .

2.11.3 Conversion ELF field → somatic depolarisation

$$\Delta V_{\text{soma}} = \alpha_{ds} \kappa \Phi B_{\text{rms}},$$

where

- $\kappa = 8.27\text{ }\mu\text{V }\mu\text{T}^{-1}$ ($\pm 7\%$ changes ΔV_{soma} by $\approx 7\%$)
- $\alpha_{ds} \approx 0.50$ is the dendrite-to-soma transfer factor,
- B_{rms} is the ELF root-mean-square magnetic field.

B_{rms} scenarios

- Urban ($\leq 200\text{ m}$ from an electrified railway): $B_{\text{rms}} = 0.15\text{ }\mu\text{T}$ at 16.7 Hz (Gajšek et al. 2016).
- Rural (Schumann background): $B_{\text{rms}} = 1\text{ pT}$ at 7.83 Hz (Nickolaenko and Hayakawa 2014).

Table 2.24 Somatic depolarisation for two contrasting environments

Location	B_{rms}	f_{ELF}	Φ	ΔV_{soma}
City ($\leq 200\text{ m}$ from railway)	$0.15\text{ }\mu\text{T}$	16.7 Hz	1.0×10^2	$6.2 \times 10^{-2}\text{ mV}$
Countryside (Schumann background)	1 pT	7.83 Hz	4.0×10^1	$1.7 \times 10^{-7}\text{ mV}$

Note: These values apply specifically to 16.7 Hz railway traction harmonics, not to the 50 Hz grid.

Constants: $\alpha_{ds} = 0.50$, $\kappa = 8.27 \mu\text{V } \mu\text{T}^{-1}$.

City $\rightarrow \Delta V_{\text{soma}} \approx 0.062 \text{ mV}$

Rural $\rightarrow \Delta V_{\text{soma}} \approx 0.17 \text{ nV}$

Example (countryside, Schumann background):

$$\Delta V_{\text{soma}} = 0.5 \times 8.27 \times 10^{-6} \times 40 \times 10^{-6} \text{ V} = 1.65 \times 10^{-10} \text{ V} \approx 0.17 \text{ nV}$$

which matches the tabulated value.

Table 2.25 Weak AC / tACS protocols can entrain cortical/hippocampal rhythms

Preparation	Phase effect	Reference
Rat hippocampal slices, weak AC fields ($\sim 10 \text{ Hz}$)	Modulation/entrainment of ongoing oscillations; phase bias at low field strengths	(Reato et al. 2010 Fig. 4C)
Rats <i>in vivo</i> , weak alternating fields	Spike-timing and network oscillations biased by subthreshold fields	(Ozen et al. 2010)
Humans, α -range tACS (EEG)	Robust α -entrainment over sensorimotor/occipital cortex	(Helfrich et al. 2014)
Review (mechanisms, cross-frequency)	Consensus on resonance/synchronisation mechanisms	(Herrmann et al. 2013)
Humans, perceptual entrainment by rhythmic stimulation	Behaviour/perception entrained to external rhythms	(Thut et al. 2011)

Field strength refers to intracranial E-field ($\mu\text{V mm}^{-1}$). For human tACS, intracranial fields are modelled to be in the $10^2\text{--}10^3 \mu\text{V mm}^{-1}$ range at 1–2 mA; exact in-brain values were not directly measured in (Helfrich et al. 2014).

2.11.4 Schumann mode 7.83 Hz — threshold-lowering factors

Assuming amplitude growth $\propto \sqrt{N}$ for $\sim 10^3$ magnetite crystals per neuron (Kirschvink et al. 1992) and $10^5\text{--}10^6$ neurons in the θ generator (Buzsáki and Draguhn 2004), the net signal scales as \sqrt{N} (Pikovsky et al. 2001). The fundamental Schumann mode has $Q \approx 5\text{--}20$ depending on ionospheric conditions, corresponding to phase coherence times of $\sim 0.1\text{--}1 \text{ s}$ (occasionally a few seconds), not days (Nickolaenko and Hayakawa 2014). However, the global thunderstorm excitation ensures long-term regularity and spectral stability of the resonance power. It is this persistent, quasi-stationary background that can provide repeated phase perturbations, even though the instantaneous phase coherence of individual wave trains is short. Thus, the short coherence of individual SR bursts does not preclude effective entrainment, since the global driver maintains a continuous 7.83 Hz background. Quantitatively, the phase-locking criterion

$(\Delta V_{\text{soma}} \geq 10^{-2} \times V_{\text{margin}})$ is not met by pT-level Schumann fields directly, even if V_{margin} is substantially reduced. Any ensemble-level entrainment at pT levels is therefore highly speculative and should be regarded as a possible but unproven mechanism (Adler 1946; Schumann and König 1954; Pikovsky et al. 2001; Nickolaenko and Hayakawa 2014). Long-term spectral stability of Schumann power, summation across large neuronal ensembles, and subthreshold stochastic effects could in principle lower the effective threshold, but such scenarios would require the theta-network to operate close to an instability (bifurcation). To our knowledge, no experimental data are currently available on ELF phase locking in such pathologically unstable networks (for example with reduced PV inhibition and impaired gamma), so these possibilities remain hypothetical and are further considered in the Discussion.

2.11.5 Sensitivity analysis

Complete $(\alpha_{\text{ds}} \times \Phi \times B_{\text{rms}})$ combinations are in Supplementary Tables S27 – S28.

The most extreme realistic urban case ($\Phi = 120$; $\alpha_{\text{ds}}=0.55$) yields $\Delta V_{\text{soma}} = 0.082$ mV.

2.11.6 Comparison with Johnson noise

For bandwidth $\Delta f = 5$ kHz and dendritic input resistance $R \approx 200$ M Ω

$$V_{\text{rms}} = \sqrt{4k_B T R \Delta f}$$

For the whole cell (capacitive approximation)

$$V_{\text{rms}} \simeq \sqrt{\frac{k_B T}{C}},$$

with $C \approx 150$ pF.

- Dendrite ($R \approx 200$ M Ω , $\Delta f = 5$ kHz): $V_{\text{rms}} \approx 130$ μ V; urban $\Delta V_{\text{soma}} \approx 62$ μ V $\approx 0.48 \times$ dendritic V_{rms} (conservative, cross-compartment comparison).
- Whole-cell ($C \approx 150$ pF): $V_{\text{rms}} \approx 5.3$ μ V; urban $\Delta V_{\text{soma}} \approx 62$ μ V $\approx 12 \times$ whole-cell V_{rms} .

Note that this is a heuristic signal-to-noise estimate comparing the RMS of a narrowband 16.7 Hz drive to broadband Johnson noise over a 5 kHz bandwidth; a full spectral SNR analysis is beyond the scope of this section.

2.11.7 Procedure and limitations

- Additivity. Amplitudes < 0.1 mV are within the linear f-I regime (Magee and Cook 2000), thus ΔV_{soma} sums linearly with other biases.

- Phase synchrony. With coherence over ≈ 10 θ cycles, injection locking of theta oscillators is in principle feasible for sufficiently strong driving fields (Adler 1946; Pikovsky et al. 2001), but pT-level Schumann fields fall far below the required amplitude (see 2.11.4).
- Conservatism. We used moderate-to-low values for the magnetite chain parameters ($Q \approx 12$, $\kappa \approx 8.27 \text{ } \mu\text{V}/\mu\text{T}$); higher Q or stronger mechano-electrical coupling would only increase Φ and ΔV , so the ΔV_{soma} values reported here are conservative lower bounds.
- Existence of crystals. The presence of ordered, biogenic magnetite chains in mammalian nervous tissue remains debated. Environmental contamination particles have been reported in human brain (e.g. Maher et al. 2016), and several critical reviews argue that evidence for magnetite-based magnetoreceptors in vertebrates is weak or ambiguous (e.g. Shaw et al. 2015). We therefore treat Φ as potentially over-estimated and, in the extreme, effectively zero in mammalian vCA1.
- Supplementary material. Detailed equations, extreme-peak (1 s) analyses and comparisons with other ELF bands are provided in Supplementary Table S30.
- In stress-primed vCA1 pyramidal cells, several changes act in the same direction to amplify the impact of a given subthreshold ΔV_{soma} . Input resistance tends to increase, KCC2 \downarrow /NKCC1 \uparrow -driven E_{GABA} depolarisation reduces shunting inhibition, EPSPs are prolonged in CREB-high neurons, PV/ γ weakening widens the coincidence window for spike generation, and the residual ΔV_{margin} itself is narrowed. Together with possible summation across many magnetite-bearing neurons, these factors imply that the ΔV_{soma} values reported here are conservative lower bounds for any phase bias in low- ΔV_{margin} networks. These considerations motivate direct experimental tests of whether such compromised networks are measurably more susceptible to weak ELF phase perturbations, or whether the effective gain remains negligible.

2.11.8 Sensitivity-analysis take-aways

- During continuous exposure, $\Delta V_{\text{soma}} \leq 0.1 \text{ mV}$; a 1-s peak ($\times 3 B_{\text{rms}}$) after dendritic RC filtering

$$|H_{RC}(f)| = \frac{1}{\sqrt{1 + (2\pi f \tau)^2}}$$

$$\tau = 20\text{-}50 \text{ ms}, \quad f = 16.7 \text{ Hz}$$

yields 0.083–0.036 mV (i.e. ~40–80 % attenuation).

- In small dendritic compartments ($R \approx 200 \text{ M}\Omega$, $\Delta f = 5 \text{ kHz}$) the urban ELF signal is $\approx 0.5\times$ the Johnson noise; at the whole-cell level ($C \approx 150 \text{ pF}$) it is $> 10\times$ larger.
- Values obtained favour a phase synchronisation (injection locking) mechanism rather than direct energy transfer.
- Persistent, quasi-stationary spectral background of Schumann modes (despite the short $\sim 0.1\text{--}1 \text{ s}$ phase coherence of individual wave trains) plus signal summation from $\approx 10^3$ crystals could in principle facilitate a slight phase bias of the θ -network even under very weak ELF backgrounds, but any such effect at pT amplitudes remains highly speculative.
- If ordered magnetite chains were present, they could in principle act as a “quartz clock” for 7–30 Hz rhythms. Within the plausible range of Φ and B_{rms} this role would be relatively robust to parameter variations, but given the lack of clear evidence for such structures in mammalian vCA1 we treat this as a speculative upper-bound scenario.
- In the torque-transducer model, the effective sensitivity κ and hence ΔV_{soma} scale approximately linearly with the number of crystals per chain; the present choice of $N \approx 10^3$ follows (Kirschvink et al. 1992) and therefore likely underestimates any larger assemblies or multiple chains per neuron.

2.11.9 Schumann-resonance specific limitations

The Schumann-resonance sub-branch of Axis F is subject to particularly strong constraints. Even under the upper-bound parameterisation in 2.11, the 7.83 Hz Schumann mode at $\approx 1 \text{ pT}$ yields ΔV_{soma} values on the order of 10^{-7} mV ($\approx 0.17 \text{ nV}$). By contrast, the phase-locking criterion in our framework is $\Delta V_{\text{soma}} \geq 10^{-2} \times V_{\text{margin}}$, which corresponds to $\approx 0.1\text{--}0.2 \text{ mV}$ for typical margins in healthy tissue and $\approx 0.05 \text{ mV}$ even for pathologically reduced $V_{\text{margin}} \approx 5 \text{ mV}$. Thus, for the fundamental Schumann mode, the effective drive amplitude remains approximately $10^5\text{--}10^6$ -fold below the threshold required for direct phase locking, even in a narrowed-margin network.

In principle, several factors could partially compensate for this extreme amplitude deficit. First, the centre frequency of the fundamental Schumann mode (7.83 Hz) lies close to the hippocampal theta band, so the detuning between the external driver and the intrinsic theta oscillator is small. In classical synchronization theory (Adler-type locking and Arnold tongues), small detuning reduces the required forcing amplitude for phase capture. Second, Schumann

fields are globally coherent and persist over very long timescales, so the number of available cycles for potential phase perturbation is enormous. Third, if a high-Q biophysical transducer (e.g. magnetite chains) exists and conserves phase information between the external field and local ΔV_{soma} , then even a very weak but phase-coherent drive could, in principle, bias the timing distribution of spikes rather than inject energy per se. Under this best-case scenario, any contribution of the 7.83 Hz mode would be restricted to networks that already operate close to an instability (critically narrowed V_{margin} , weakened PV/gamma control, prolonged coincidence windows) and would manifest only as a subtle phase bias, not as a robust trigger of replay or spikes.

However, none of the required conditions has been empirically demonstrated in chronically stressed human vCA1. Existing EEG–Schumann studies have focused on healthy participants and macroscopic spectral correlations, and report at best weak and inconsistent convergence between alpha/theta bands and the Schumann spectrum. They do not directly address the conditional, micro-level mechanism modelled here (magnetite-like transduction, theta/gamma instability, ensemble summation over many cycles). Likewise, potential facilitatory effects of gamma weakening (for example under THC) on phase sensitivity to ELF fields are treated in EMM as qualitative, mechanistically plausible pathways rather than as established phenomena.

For these reasons, within the present EMM the 7.83 Hz Schumann mode is treated only as a boundary-case phase perturbation. It cannot act as a stand-alone driver of replay or symptoms and plays a role, if any, only in already compromised, low- ΔV_{margin} networks as a very weak modulator of theta phase. The epidemiological β -loop is therefore framed to adjudicate only whether short-term ELF/geomagnetic variability shows any reproducible association with clinical endpoints; it cannot validate or refute the Schumann-specific microscopic mechanism, which remains strictly hypothetical and requires dedicated future biophysical and MEG/EEG studies.

2.12 Electrotonic cascade (layered multipliers)

This section documents only the calculation workflow that yields the cumulative values presented in 3.8. All primary sources, sensitivity matrices and spreadsheets are in Supplementary Tables S31 – S32.

2.12.1 Baseline data for a vCA1 pyramidal cell

Table 2.26 Baseline parameters (P35 – P50, mouse)

Quantity	Value (mean \pm SD)	Source
V_{rest}	-71.1 mV	(Cembrowski et al. 2016a)

V_{thr}	-50.9 mV	(Cembrowski et al. 2016a)
Rheobase	$140 \pm 10 \text{ pA}$	(Pignatelli et al. 2019; Fig. 1E)
R_{in} (vCA1)	$110 \pm 8 \text{ M}\Omega$ SD = SEM $\times \sqrt{n} \approx 8 \text{ M}\Omega$ ($n = 14$).	(Milior et al. 2016; Suppl. Fig. S1b)
τ_{EPSP}	$15 \pm 1 \text{ ms}$	(Magee 1999)
IPSC _{PV→pyr} (norm.)	1.0	(Gulyás et al. 1999)

2.12.2 Layered excitability budget — worked example (CACNA1C rs1006737 A)

Table 2.27 Relative changes across successive layers

Layer	Principal trigger	$\Delta V_{\text{rest}} [\text{mV}]$	Rheobase [%]	$\tau_{\text{EPSP}} [\%]$	$R_{\text{in}} [\%]$	IPSC _{PV→pyr} [%]
1	CRS / CUS $\geq 14 \text{ d}$	+11.3	-44	+15	+29	-16
2	CACNA1C rs1006737 A	0	-6	+15	0	0
3	Hot spot (CREB-high cluster)	+3.2	-15	+25	—	—
4	Minute-to-hour bias (caffeine, nicotine, ROS etc.)	+0.5 → +3	—	—	—	—

Layer 4 affects only V_{margin} additively and does not modify passive parameters.

2.12.3 Combining percentage changes

Parameters are combined multiplicatively, not additively:

$$\text{Combined factor} = \prod_{i=1}^n \left(1 + \frac{\Delta_i}{100}\right),$$

where Δ_i is the percentage change in layer i (Fricker and Miles 2000; Magee and Cook 2000).

2.12.4 Resulting multipliers and absolute values (CACNA1C case)

Table 2.28 Cumulative multipliers and scaled values

Axis	CRS	CACNA1C	Hot spot	Combined factor	Baseline	After stacking	Net change %
Rheobase	-44 %	-6 %	-15 %	$0.56 \times 0.94 \times 0.85 = 0.447$	140 pA	63 pA	-55 %
R_{in}	+29 %	0 %	+0 %	$1.29 \times 1.00 \times 1.00 \approx 1.29$	110 MΩ	142 MΩ	+29 %
τ_{EPSP}	+15 %	+15 %	+25 %	$1.15 \times 1.15 \times 1.25 \approx 1.65$	15 ms	24.8 ms	+65 %
IPSC _{PV→pyr}	-16 %	0 %	-0 %	$0.84 \times 1.00 \times 1.00 = 0.84$	1.00	0.84	-16 %

Percentage changes are combined multiplicatively and are not summed into $\Sigma \Delta V_{\text{margin}}$ (which is computed separately in mV).

Step-by-step example – rheobase

Baseline: 140 pA (Pignatelli et al. 2019) (dCA1, 34 °C); the dorsal–ventral difference is < 5 %, therefore the error is $< \pm 7 \text{ pA}$.

1. Layer 1 (-44%): $140 \times 0.56 = 78$ pA.
2. Layer 2 (-6%): $78 \times 0.94 = 74$ pA.
3. Layer 3 (-15%): $74 \times 0.85 = 63$ pA

Combined σ (layer-wise RSS over the multiplicative pipeline):

$$\sqrt{(17 \times 1.0)^2 + (6 \times 0.56)^2 + (15 \times 0.526)^2} \approx 19 \text{ pA}.$$

Including the baseline measurement SD (± 10 pA) in quadrature gives ≈ 21 pA.

The same algorithm was applied to R_{in} , τ_{EPSP} and $IPSC_{PV \rightarrow pyr}$.

Functional consequences

- Rheobase $\downarrow 55\%$ \rightarrow firing threshold ≈ 63 pA.
- $R_{in} \uparrow 29\%$ \rightarrow neurons respond to smaller synaptic currents.
- $\tau_{EPSP} \uparrow 65\%$ \rightarrow temporal summation window extends to ≈ 25 ms.
- Shunt PV $\downarrow 16\%$ \rightarrow weaker perisomatic inhibition.

2.12.5 Notes and limitations

- All values are from mice P35 – P50; when sex differences existed, the lower male R_{in} was used (conservative).
- Layer-4 bias (0.5 – 3 mV) does not affect passive parameters; it adds only to V_{margin} .
- Uncertainties were combined in Supplementary Table S32 by root-sum-of-squares.
- The *SCN2A R1882Q* scenario follows the same pipeline (see Suppl. Table S32B).
- $\sigma = 17\%$ for layer 1 (MacKenzie and Maguire 2015), after scaling this gives 13 pA—a conservative upper estimate.
- Baseline rheobase. To date, no direct measurements of rheobase for ventral CA1 pyramidal neurons at 34 °C (P35 – P50 mice) have been published. We therefore adopted the value reported for dorsal CA1 under identical recording conditions (138 ± 9 pA; (Pignatelli et al. 2019)). The dorsal–ventral difference in rheobase at 32 °C is $< 5\%$ (Dougherty et al. 2012); we thus apply a conservative $\pm 5\%$ tolerance to this baseline. Should a vCA1-specific measurement at 34 °C become available, the 140 pA baseline can be replaced directly without altering the multiplicative framework used to combine percentage changes.

2.13 Network transients that may synchronise with an ELF phase

Table 2.29 Network transients in ventral CA1 of the mouse (RUN state)

Transient	Event density λ [min $^{-1}$]	Time window t [ms]	Baseline LFP amplitude (p-p, mV)	Key sources
θ oscillation (7–10 Hz)	≈ 2400 windows min $^{-1}$ (4 quadrants · cycle)	100–140	1.0	(Lubenov and Siapas 2009 Fig. 2C; Nuñez and Buño 2021 Fig. 1B)
Sharp wave + ripple (140–200 Hz)	1.9 events min $^{-1}$	50–120 (mean 100)	$0.22 \pm 0.14^\dagger$	(Ylinen et al. 1995; Liu et al. 2022 Fig. 2F; Schieferstein et al. 2024)

† Mean SWR amplitude is 0.22 mV (Schieferstein et al. 2024; Fig. 3E). A value of 0.40 mV (\approx 65th percentile of the distribution) is adopted to avoid underestimating the contribution of stronger events. Rare “mega SWRs” > 1 mV (English et al. 2014 Fig. 4D; Roux et al. 2017) are omitted. The 0.40 mV value corresponds to the upper tertile (visual estimate from the distribution).

Event density for θ is estimated from cycle frequency (8–10 Hz) multiplied by four quadrants per cycle; source papers provide θ frequency but not explicit event counts. (The 100–140 ms window corresponds to one full θ cycle at 7–10 Hz ($t = 1/f$)).

The 1.0 mV θ amplitude is chosen as a conservative lower-bound representative value within typical hippocampal θ LFP ranges. In vitro recordings of cholinergic theta in hippocampal slices report amplitudes of 0.1–2 mV at 4–12 Hz (Kowalczyk et al. 2013), and in vivo depth profiles in mouse hippocampus show the largest-amplitude theta waves > 1 mV at the hippocampal fissure (Buzsáki et al. 2003). Thus 1.0 mV is a conservative choice for CA1 pyramidal-layer θ .

The nominal 100 ms window corresponds to the average duration of the entire sharp-wave–ripple complex (Ylinen et al. 1995).

LFP $\rightarrow \Delta V_{\text{soma}}$ conversion

For SWRs, (English et al. 2014; Fig. 4C–D) show that peak-to-peak LFP approximates somatic depolarisation under I_h block (pharmacological: ZD7288; genetic: HCN1 knock-out). (English et al. 2014) show that under reduced I_h , larger ripple LFP amplitudes are accompanied by proportionally larger somatic depolarisations, consistent with using ripple LFP amplitude as a proxy for ΔV_{soma} . For θ (8–10 Hz) we assume order-of-magnitude equivalence (low-frequency transfer is favourable), which is within the empirical variability and included in the sensitivity analysis (Supplementary Tables S33–S34).

See also theoretical and modelling work on how subthreshold membrane conductances and multineuronal V_m dynamics shape LFPs in CA1 and cortex (Herreras 2016; Ness et al. 2016; Noguchi et al. 2023).

2.13.1 Activity-scaling factors after CRS + hot spot + CACNA1CA

R_{in} increase $\rightarrow +29\%$ (combined electrotonic cascade; see Table 2.18), $k_R = 1.29$.

For θ (~ 8 Hz), a simple RC model (Harvey et al. 2009; Zemankovics et al. 2010) yields an effective $k_{R(\theta)} = \sqrt{1.29} \approx 1.11$, rounded to 1.10. The numerical value (1.10) is model-derived; the cited papers provide the impedance profile and τ values, not the exact coefficient. Theoretically, $k_{R(\theta)} \approx 1.06\text{--}1.09$ for 8–10 Hz from the same RC approximation; we use 1.10 as a conservative, transparently rounded value.

At 150 Hz ($\omega\tau \gg 1$), the RC filter suppresses R_{in} effects, therefore $k_{R(SWR)} = 1.00$.

PV shunt reduction: -16% (layer 3; from the vCA1 hot spot + CACNA1CA model, see Section 2.9 / Table 2.18) weakens perisomatic inhibition.

For ≤ 10 Hz we adopt $k_{PV} = 1.10^*$ (Booth and Rinzel 1995). The value 1.10 is model-derived within the divisive-inhibition framework of (Booth and Rinzel 1995), rather than directly measured.

Above ~ 60 Hz the perisomatic IPSC influence on somatic V_m diminishes; at ~ 150 Hz we consider the shunt negligible and set $k_{PV(SWR)} = 1.00$, consistent with the time course of PV IPSCs relative to the ripple period.

Table 2.30 Final somatic depolarisation

Transient	ΔV_{base} [mV]	k_R	k_{PV}	ΔV_{soma} [mV]
θ	1.00	1.10	1.10	1.21
SWR	0.40	1.00	1.00	0.40

$$\Delta V_{soma} = \Delta V_{base} \cdot k_R \cdot k_{PV}.$$

Baseline ΔV values represent physiologically typical amplitudes consistent with ranges in CA1 pyramidal neurons; exact values are not explicitly reported in the cited papers but fall within known variability.

All derivations and sensitivity tests are provided in Supplementary Tables S33–S34.

2.13.2 Notes and limitations

Current calculations include only the two best characterised transients (θ oscillations and SWRs), because frequency and duration are well constrained and amplitude can be placed within physiologically typical CA1 ranges. Future versions of the model can incorporate

additional high-amplitude events—e.g. dentate bursts or entorhinal layer II gamma—once reliable quantitative data on their occurrence become available. These could be added linearly to the depolarisation budget, proportionally increasing the overall chance of ELF phase alignment.

2.14 Phase-locking model

We calculate the probability (P_{phase}) that, within a 25 ms EPSP-summation window, the peak of at least one of three independent ELF bands (7.83 Hz; 16–18 Hz; 20–28 Hz) occurs, and we derive the urban–rural gradient $G = P_{phase,city} / P_{phase,village}$.

Complete data sheets and sensitivity analyses are provided in Supplementary Tables S35 – S40.

2.14.1 Input assumptions

1. Integration window $\Delta t = 25$ ms ($\approx \tau_{EPSP,\text{eff}} - 2.12.4$).
2. Global band The Schumann fundamental at 7.83 Hz is present everywhere.
3. Urban additions Large settlements add traction-related 16–18 Hz and industrial 20–28 Hz bands.
4. Band weights (f_i) and periods (T_i) are listed in Supplementary Table S35.
5. Because no measurements of phase correlation between the independent ELF bands are available, we assumed phase independence ($|r| < 0.05$) and performed a sensitivity analysis for $r = 0.02–0.10$ (Supplementary Table S39).
6. If $\Delta t < T_i \rightarrow p_i = \Delta t/T_i$; when $\Delta t \geq T_i \rightarrow p_i = 1$.
7. In the sensitivity run, residual correlations are down-weighted by $\rho = 1 - r$ (Supplementary Table S39).

Table 2.31 Prevalence of dominant ELF bands

Region / study	n recordings	Dominant band	Sites affected
(Brix et al. 2001; Fig. 10; Tab. 4)	1952 individuals, 24-h personal recording	16–18 Hz	61 % (59–63 %) – fraction of measurement locations or 24 h recordings in which the band was clearly detectable.
(Paniagua et al. 2007; Tab. 2)	117 points	18–25 Hz	17 %
(Loizeau et al. 2024; Fig. 3b) („occurrence ratio”)	MF monitoring	16.7 Hz	62 %
(Gajšek et al. 2016; Sec. 3.2 („20–30 Hz present in 19 / 74 studies”))	74 surveys	20–28 Hz	≈ 25 %

2.14.2 Formulas

$$P(\Delta t) = 1 - \prod_{i=1}^n \left(1 - f_i \frac{\Delta t}{T_i}\right), \quad 0 < \Delta t < \min T_i.$$

$$G = \frac{P_{\text{phase,city}}}{P_{\text{phase,village}}}$$

2.14.3 Numerical procedure ($\Delta t = 25 \text{ ms}$)

Insert p_i values → Supplementary Tables S36–S37.

Compute $P_{\text{phase, city}}$ and $P_{\text{phase, village}}$.

Derive gradient G → Supplementary Table S38.

95% CI: varying each input (f_i, p_i) by $\pm 10\%$ and sampling 2^6 extreme combinations; we report the resulting minimum and maximum P_{phase} values.

$$P_{\text{phase, city}} = 1 - \prod_i (1 - f_i p_i) = 1 - (0.805)(0.740)(0.894) \approx 0.467$$

For rural areas (only the 7.83 Hz mode):

$$P_{\text{phase, village}} = f_1 p_1 = 1.00 \times 0.195 = 0.195$$

Table 2.32 Window-width sensitivity

Δt	$P_{\text{phase,city}}$	$P_{\text{phase,village}}$	Gradient (G)
20 ms	0.387	0.156	2.48
25 ms	0.467	0.195	2.40
30 ms	0.539	0.234	2.30

2.14.4 Derivation and monotonicity proof for $P_{\text{phase}}(\Delta t)$

For independent bands $i = 1 \dots n$:

$$\ln[1 - P(\Delta t)] = \sum_{i=1}^n \ln\left(1 - f_i \frac{\Delta t}{T_i}\right).$$

First derivative:

$$\frac{d}{d\Delta t} \ln[1 - P] = - \sum_{i=1}^n \frac{f_i}{T_i \left(1 - f_i \frac{\Delta t}{T_i}\right)} < 0.$$

Thus $dP/d\Delta t > 0$; P increases with Δt . The gradient $G = P_{\text{city}} / P_{\text{village}}$ decreases with Δt for $n \geq 3$ because the denominator (single band) grows faster. Formally:

$$\frac{dG}{d\Delta t} = \frac{P'_{\text{city}} P_{\text{village}} - P_{\text{city}} P'_{\text{village}}}{P_{\text{village}}^2} < 0, \quad n \geq 3.$$

Using $\sum_{i \geq 2} f_i > 0$ for urban sites.

Frequencies 50–60 Hz ($T \approx 20$ ms) do not resonate with biogenic magnetite and do not differentiate locations, so they are omitted.

2.14.5 Term definitions

P_{phase} — probability that within a 25-ms EPSP window at least one ELF peak occurs in a band centred at 7.83 Hz, 16–18 Hz or 20–28 Hz.

Gradient = $P_{\text{phase,city}} / P_{\text{phase,village}}$.

2.14.6 Methodological notes

For the industrial 20–28 Hz band we use an effective period $T = 42.5$ ms, i.e. the weighted mean of the band limits ($20 \text{ Hz} \rightarrow 50 \text{ ms}; \quad 28 \text{ Hz} \rightarrow 35 \text{ ms}$). This yields $p_3 = \Delta t/T = 25 \text{ ms} / 42.5 \text{ ms} \approx 0.588$ (see Supplementary Table S36).

To date, no studies have quantified the instantaneous (phase) correlation between the 7.83 Hz, 16–18 Hz and 20–28 Hz ELF bands at the same site. In the absence of such data we adopt a maximum-entropy scenario.

For the industrial 20–28 Hz band, we set $f_{20} = 0.18$ based on urban spot measurements in Cáceres, Spain, where 18–25 Hz components were detectable at 17% of measurement points (Paniagua et al. 2007; Tab. 2). This is consistent with a European review reporting 20–30 Hz components in 19 out of 74 environmental ELF-MF studies (~25%) (Gajšek et al. 2016), which we here interpret as an approximate upper bound on the fraction of urban or industrial settings where this band is present.

For the 20–28 Hz band, the fraction f_{20} should be interpreted as a proxy for the fraction of urban or industrial environments where this band is detectable, rather than a literal land-area fraction; we therefore treat it as an order-of-magnitude estimate and explore its variation in the sensitivity analysis.

2.15 Algorithm for estimating the rate of θ + SWR coincidences corrected for ELF phase

2.15.1 General assumptions

Example scenario: CACNA1C rs1006737 A.

Postsynaptic integration window: $\Delta t = 25$ ms $\tau_{\text{EPSP,eff}} \approx 24.8$ ms; (Magee and Cook 2000).

Transients considered:

θ oscillation (4 quadrants per cycle);

sharp-wave + ripple (SWR) — the θ -associated ripple (TAR) in mice; the same definition is applied to humans.

ELF-band independence: No phase-correlation data exist; we therefore assume maximal entropy (independence). For $r = 0.02 - 0.10$ the impact on the gradient G stays $< 10\%$ (Supplementary Table S39).

Phase-alignment factors from 2.14:

$$P_{\text{phase, city}} = 0.467$$

$$P_{\text{phase, village}} = 0.195$$

Effective SWR duration:

$$t_{\text{eff,SWR}} = t_{\text{SWR}} + (\tau_{\text{EPSP,eff}} - 15 \text{ ms})$$

where 15 ms is taken as the typical lag between the SWR trough and half-decay of the somatic EPSP. For $t_{\text{SWR}} \approx 100$ ms we obtain $t_{\text{eff,SWR}} \approx 110$ ms.

Note: t_{SWR} refers to the entire SPW-R complex; ripple durations alone are shorter (typically $\sim 70-90$ ms in human recordings and 50–100 ms in rodents) (Ylinen et al. 1995; Dickey et al. 2022).

2.15.2 Baseline parameters

Table 2.33 Baseline values used in 2.15

Parameter	Mouse (RUN)	Human — rest (fast θ 6–8 Hz)	Human — slow walk (8–9 Hz)	Human — β / high- θ (15–18 Hz)	Source
f_θ [Hz]	10	7	8.8	16	Mouse: (Fernández-Ruiz et al. 2017 Fig. 2B). Human: (M. Aghajan et al. 2017 Fig. 3G; Goyal et al. 2020; Pfeffer et al. 2022; Radetz and Siegel 2022 4A-C)
λ_{SWR} [min^{-1}]	1.9 (1.8–2.1)	1.2 (0.9–1.5)	0.9 (0.4–1.5)	0.8 (β -mod.)	Mouse: (Liu et al. 2022a) Human: (Chen et al. 2021; Norman et al. 2021; Liu et al. 2022b; Radetz and Siegel 2022; Iwata et al. 2024)

t_{SWR} [ms]	100 (80–120)	100	100	100	(Ylinen et al. 1995 Tab. 1; Jiang et al. 2020; Schieferstein et al. 2024)
$\tau_{\text{EPSP,eff}}$ [ms]	24.8 ± 1.0	24.8	24.8	24.8	(Magee 1999; Magee and Cook 2000 Fig. 3D)

Complete parameter lists are in Supplementary Tables S41 (mouse) and S42 (human).

f_θ values are representative within the ranges reported by the cited studies rather than exact sample means.

95% CI: each input parameter (f_θ , λ_{SWR} , t_{SWR}) was perturbed by $\pm 10\%$; we sampled a grid of extreme combinations and report the resulting minimum and maximum N_{hit} values (Supplementary Table S43).

The λ_{SWR} values in humans are chosen from the lower part of the waking ripple rate ranges reported in (Chen et al. 2021; Norman et al. 2021) and related studies, in order to avoid inflating N_{hit} .

Effective somatic EPSP decay constant $\tau_{\text{decay}} = 24.8 \pm 1$ ms at 34 °C (Magee and Cook 2000; Fig. 3d).

Published waking SWR rates span 0.5 – 40 events min⁻¹ depending on detection threshold; we use the 10th–20th percentile values to avoid inflating N_{hit} .

Fast-θ (6–9 Hz) occasionally appears during quiet wakefulness with eyes open (Goyal et al. 2020; Fig. 1E); we therefore model rest at 7 Hz.

This 15–18 Hz rhythm corresponds to the arousal-linked beta/‘high-theta’ reported by (Radetz and Siegel 2022) (MEG) and (Pfeffer et al. 2022); hippocampal coupling is assumed via septo-thalamo-cortical drive.

Value = 10th percentile of awake ripple distribution in consensus SPW-R (Liu et al. 2022a), chosen to avoid overestimating N_{hit} .

2.15.3 Formulas

1. θ-window width: $\Delta t_\theta = 1/(4f_\theta)$
2. Number of θ-windows per minute: $\lambda_{\theta,\text{window}} = 4f_\theta \times 60$
3. Total overlap time: $t_{\text{sum}} = t_{\text{eff,SWR}} + \Delta t_\theta$
4. Probability of a single hit

$$p_{\text{hit}} = \lambda_{\text{SWR}} \frac{t_{\text{sum}}}{60}$$

5. Raw hit count

$$N_{\text{hit,raw}} = p_{\text{hit}} \times \lambda_{\theta,\text{window}}$$

6. ELF-phase correction

$$N_{\text{hit,city}} = N_{\text{hit,raw}} \times 0.467$$

$$N_{\text{hit,village}} = N_{\text{hit,raw}} \times 0.195$$

2.15.4 Calculation steps

Mouse (vCA1, RUN state)

$$f_\theta = 10 \text{ Hz} \rightarrow \Delta t_\theta = 25 \text{ ms}; \quad \lambda_{\theta-\text{window}} = 2400 \text{ min}^{-1}.$$

$$\lambda_{\text{SWR}} = 1.9 \text{ min}^{-1}.$$

$$t_{\text{sum}} = 110 \text{ ms} + 25 \text{ ms} = 135 \text{ ms}.$$

$$p_{\text{hit}} = 1.9 \times 0.135 / 60 = 0.00428.$$

$$N_{\text{hit,raw}} = 0.00428 \times 2400 = 10.26 \text{ min}^{-1}.$$

$$N_{\text{hit,city}} = 10.26 \times 0.467 = 4.79 \text{ min}^{-1}.$$

$$N_{\text{hit,village}} = 10.26 \times 0.195 = 2.00 \text{ min}^{-1}.$$

→ Results summarised in Supplementary Table S41.

Human — three waking scenarios

Input values and outputs are in Supplementary Table S42; example for rest ($f_\theta = 7 \text{ Hz}$, $\lambda_{\text{SWR}} = 1.2 \text{ min}^{-1}$):

$$\Delta t_\theta = 35.7 \text{ ms}; \quad \lambda_{\theta-\text{window}} = 1680 \text{ min}^{-1}.$$

$$t_{\text{sum}} = 110 + 35.7 = 145.7 \text{ ms}.$$

$$p_{\text{hit}} = 1.2 \times 0.1457 / 60 = 0.00291.$$

$$N_{\text{hit,raw}} = 0.00291 \times 1680 = 4.90 \text{ min}^{-1}.$$

$$N_{\text{hit,city}} = 4.90 \times 0.467 = 2.29 \text{ min}^{-1}.$$

$$N_{\text{hit,village}} = 4.90 \times 0.195 = 0.96 \text{ min}^{-1}.$$

Identical calculations were performed for “slow walk” and “β arousal”.

2.15.5 Interpretation

Mean depolarisation per packet (mouse):

$$\Delta V_{\text{packet}} = 1.21 \text{ mV} + 0.40 \text{ mV} = 1.61 \text{ mV}.$$

Urban–rural gradient for both mice and humans is ≈ 2.4 , identical to that of P_{phase} alone—because the ELF correction scales N_{hit} linearly.

t_{sum} – expressed in seconds; λ_{SWR} in events · min⁻¹

$\lambda_{\theta\text{-window}}$ – number of θ -quadrants per minute

2.16 Geomagnetic storms as a modulator of the global “phase clock”

2.16.1 Physical chain — from the geomagnetic field to membrane depolarisation

1. Induction vectors. The rms amplitude of the fundamental Schumann mode (7.83 Hz) at mid-latitudes averages $B_{\text{rms}} \approx 0.3 \text{ pT}$ on quiet days (range 0.25–0.4 pT) and $\approx 3 \text{ pT}$ during $K_p \geq 6$ storms (range 2–4 pT) (Sátori et al. 2007).
2. Field-to-voltage conversion. Voltage induced across a magnetite chain: $\Delta V = \kappa B_{\text{rms}}$, $\kappa = 8.27 \mu\text{V} \mu\text{T}^{-1}$ (Kirschvink 1996) chap. 12, tab. 2, p. 242.
3. Phase gain. Magnetite chains of $\sim 10^3$ crystals provide an effective phase gain in the 7–20 Hz band of $\Phi \approx 40$ (range 30–60), consistent with direct measurements (Kirschvink et al. 1992; Winklhofer and Kirschvink 2010). We adopt $\Phi = 40$ as the nominal value and test 30/60 in sensitivity analyses (2.11.2; Supplementary Table S26).
4. Dissipative loss. Dendrite → soma current reduction: $\alpha_{\text{ds}} = 0.50$ (Golding et al. 2005).
5. Somatic depolarisation.

$$\Delta V_{\text{soma}} = \kappa B_{\text{rms}} \Phi \alpha_{\text{ds}} \approx 5 \times 10^{-8} \text{ mV} \text{ (quiet)} \text{ vs } 5 \times 10^{-7} \text{ mV} \text{ (storm)}$$

Both values are $< 10^{-4} \%$ of a single-EPSP amplitude (0.5 mV), confirming that the Schumann wave acts purely as a phase cue. (Numerical details → Supplementary Table S44). Values of κ and Φ are taken from order-of-magnitude estimates in (Kirschvink 1996; Winklhofer and Kirschvink 2010); even if both were doubled, the induced ΔV_{soma} would remain $\ll 10^{-3} \%$ of a typical EPSP.

2.16.2 Phase-window narrowing during a storm

ELF magnetometers show a reduction in the full width at half maximum (FWHM) of the 7.83 Hz peak:

- $\Delta \text{FWHM} \approx 9 \%$ Nagycenk 47°N; 30 storm $K_p \geq 6$; (Sátori et al. 2007; Fig. 5b)
- $\Delta \text{FWHM} = 11 \%$ station Querétaro, 19–25° N; (Pazos et al. 2019; Fig. 7) (10–12 %)
- $\Delta \text{FWHM} 14.7 \%$ Sierra Nevada, 30–37° N; (Rodríguez-Camacho et al. 2022; Fig. 6d)

Mean $\Delta \text{FWHM} \approx 11 \%$ →

$$\Delta\varphi \approx \pi \frac{11\%}{100\%}, g_{\text{full}} = \frac{\Delta\varphi}{\pi/2} \approx 0.22.$$

Conservative variant (main analysis).

To avoid overestimation we take $g_{\text{coh}} = 0.13 \pm 0.02$ ($\pm 6.5\%$ narrowing, $\approx 60\%$ of the mean effect).

$$g_{\text{coh}} = \frac{\Delta\varphi}{\pi/2} \approx 0.13 \pm 0.02.$$

Full variant ($g = 0.22$)—the average narrowing—raises $P_{\text{phase, city}}$ to 0.612; when combined with 2.16.5 this implies $\text{RR} \approx 1.33$ (see Supplementary Table S45B + 2.16.5).

2.16.3 Updated probability for a 7.83 Hz peak

Base probability within $\Delta t = 25$ ms:

$$p_{7.83} = \frac{\Delta t}{T} = \frac{25}{128} = 0.195.$$

During a storm:

$$p_{7.83}^{\text{storm}} = 0.195 + 0.13 = 0.325.$$

Mapping FWHM narrowing to probability increment g (addition to p) is a modelling assumption; the multiplicative variant $p(1+g)$ is presented in Supplementary Table S45B.

P_{phase} probabilities (formula 2.14):

$$P_{\text{phase}} = 1 - \prod_i (1 - f_i p_i).$$

Result: 0.553 (city) / 0.325 (village) — Table S45.

The difference between calculating $p_{\text{storm}} = p + g$ versus $p_{\text{storm}} = p(1+g)$ is about 0.10 points (32% relative), which lies within the uncertainty bounds of g .

We adopt the additive mapping $p + g$ as a conservative assumption; the multiplicative variant $p(1 + g)$ is presented in Supplementary Table S45B for comparison.

We assume that an 11 % reduction in the FWHM of the 7.83 Hz peak translates into an equivalent relative narrowing of the admissible phase interval, and we encode this as an additive increase g in $p_{7.83}$. This mapping is heuristic and is therefore explored in both additive and multiplicative variants (Supplementary Table S45).

2.16.4 Re-computing the $\theta + SWR + ELF$ hit rate

Resting baseline $N_{\text{hit,raw}} = 4.90 \text{ min}^{-1}$ (2.15).

$$N_{\text{hit,city}} = 4.90 \times P_{\text{phase,city}}, \quad N_{\text{hit,village}} = 4.90 \times P_{\text{phase,village}}$$

Table 2.34 Increase in hit rate during a geomagnetic storm

Condition	P_{phase}	$N_{\text{hit}} (\text{city})$	$N_{\text{hit}} (\text{village})$
Normal	0.467 / 0.195	2.29 min^{-1}	0.96 min^{-1}
Storm	0.553 / 0.325	2.71 min^{-1}	1.59 min^{-1}

Weighted average (60% city): $0.6 \cdot 2.29 + 0.4 \cdot 0.96 = 1.76 \text{ min}^{-1}$; during storm: $0.6 \cdot 2.71 + 0.4 \cdot 1.59 = 2.26 \text{ min}^{-1}$ ($\approx +29\%$).

For the illustrative population-level weighting we assume that $\approx 60\%$ of the population lives in urban environments, close to current global estimates.

2.16.5 Micro \rightarrow macro scaling

Meta-analytic multiplier

$$\beta = \frac{RR - 1}{\Delta N_{\text{hit}}/N_{\text{hit}}}$$

from eight studies (Supplementary Table S46) gives median $\beta = 0.66$ (leave-one-out range $0.62 - 0.70$).

With $\frac{\Delta N_{\text{hit}}}{N_{\text{hit}}} = 0.28$

$$RR_{\text{hosp}} \approx 1 + 0.67 \times 0.28 \approx 1.19$$

$RR \approx 1.19$ (95 % CI with $\Delta = 0.28$: $1.13 - 1.24$). Sensitivity $\pm 15\%$ on Δ and β is in Supplementary Table S47.

Eight studies yield a pooled $\beta \approx 0.69$ (DerSimonian–Laird random-effects; 95 % CI 0.48–0.85; Table 2.35). The exact median of the individual β estimates is 0.66. For simplicity we use $\beta = 0.67$ throughout the manuscript; choosing 0.69 instead would change the final RR_{hosp} estimate by only ≈ 0.002 .

In 2.11 we use a conservative global median of 1 pT; in 2.16 we report observational ranges for mid-latitude stations: $\sim 0.25 - 0.4$ pT on quiet days and $\sim 2 - 4$ pT during $K_p \geq 6$ storms.

We adopt a 48 h operational window, consistent with the majority of studies reporting effects within 0–2 days; harmonisation does not alter β relative to the chosen Δ .

2.16.6 Heterogeneity of the β meta-analysis

2.16.6.1 Input data

All studies classified geomagnetic storm days (operationally: thresholds in $K_p \geq 6$ or $A_p \geq 60$; in several studies equivalent measures such as Dst were applied). In the meta-analysis we treat these consistently as ‘storm days’ according to the original study definition.

For each study:

$$\theta_i = \ln(RR_i), \quad Var_i = \left(\frac{\ln(CI_{upper,i}) - \ln(CI_{lower,i})}{2 \times 1.96} \right)^2.$$

Variance was computed by Mantel–Haenszel when only counts were available.

Endpoints are heterogeneous (psychiatric, cardiac, neurological), but were deliberately aggregated as a macroscopic ‘general health cost’ of geomagnetic storms.

2.16.6.2 Q statistic & I^2

Fixed-effect weights

$$w_i = \frac{1}{Var_i}.$$

Cochran’s Q statistic

$$Q = \sum_{i=1}^k w_i (\theta_i - \bar{\theta})^2, \quad \text{where } \bar{\theta} = \frac{\sum w_i \theta_i}{\sum w_i}, \quad df = k - 1.$$

Higgins–Thompson inconsistency index (Higgins and Thompson 2002):

$$I^2 = \max \left(0, \frac{Q - df}{Q} \right) \times 100\%.$$

2.16.6.3 Random-effects model

The pooled multiplier β was estimated with the DerSimonian–Laird (DL) method:

$$\tau^2 = \max \left(0, \frac{Q - df}{\sum w_i - \sum w_i^2 / \sum w_i} \right), \quad w_i^* = \frac{1}{Var_i + \tau^2}, \quad \theta_{DL} = \frac{\sum w_i^* \theta_i}{\sum w_i^*}.$$

$$\beta_{DL} = \frac{e^{\theta_{DL}} - 1}{\Delta N_{hit} / N_{hit}}, \quad \frac{\Delta N_{hit}}{N_{hit}} = 0.28$$

2.16.6.4 Results

Table 2.35 Heterogeneity statistics for β meta-analysis (random-effects model)

Measure	Value
Q (df=6)	4.25
p-value Q	0.64
I^2	0 %

τ^2 (DL)	0
β_{pooled} (DL)	0.69
95 % CI β_{pooled}	0.48–0.85

Leave-one-out analysis: β_{pooled} ranged from 0.62 to 0.70.

Lowest value after omitting (Kay 1994): $\beta = 0.62$

Highest value after omitting (Shaposhnikov et al. 2014): $\beta \approx 0.70$

Because $I^2 = 0\%$, all subsequent inference is based on the random-effects model. The constancy of β_{pooled} when each study is removed in turn confirms that the central estimate ($\beta \approx 0.69$) is not driven by any single dataset.

2.17 Rheobase and day-to-day minute–hour biases

Table 2.36 Minute–hour biases — input assumptions

Quantity	Value used in calculations	Source / comment
V_{thr} (scenario)	5.7 mV	see 3.8 (cumulative ΔV_{margin})
Baseline rheobase	140 pA	(Pignatelli et al. 2019)
Layer-1-to-3 multiplier	$0.56 \times 0.94 \times 0.85 = 0.447$	derived in 2.12.4
ΔV_{bias} — caffeine ≈ 100 mg (240 ml drip coffee)	+1 mV	GIRK block + \uparrow cAMP (Supplementary Table S23)

A full $\pm 10\%$ spread of all inputs is given in Supplementary Table S48 ($V_{\text{thr}} = 5.7$ mV).

Caffeine dose. Two standard filtered coffees 240 ml; ~ 100 mg caffeine (EFSA Panel on Dietetic Products, Nutrition and Allergies (NDA) 2015). Derivation of ΔV_{bias} .

Slope $2.5\% \mu\text{M}^{-1}$ for GIRK blockade $0\text{--}10 \mu\text{M}$ (Lopes et al. 2019) $R^2 = 0.94 \rightarrow$ estimated CSF caffeine after one 240 ml filtered coffee $\approx 5 \mu\text{M} \rightarrow$ GIRK conductance $\downarrow \approx 12\% \rightarrow \Delta V_{\text{raw}} \approx 0.83$ mV $\rightarrow \Delta V_{\text{soma}} \approx +1$ mV after applying $k_R \cdot k_{\text{PV}} = 1.21$.

Final step (“ -55% rheobase”). The current threshold is converted to an equivalent reduction of the effective excitability margin in mV using the Lapicque formulation (not merely $V_{\text{thr}} - V_{\text{rest}}$).

The 95 % confidence interval of the margin partially overlaps the packet amplitude, yet the mean excess remains positive.

2.18 Assumptions and modelling procedures for the fear (SZ), sadness (MDD) and trauma (PTSD) loops

In the final step of the model we construct three qualitative loops that describe how chronic replay of a threat-biased vCA1 engram can drive network-level trajectories towards schizophrenia (SZ), major depressive disorder (MDD) or post-traumatic stress disorder (PTSD). All numerical values in Supplementary Tables S49–S51 are mean changes relative to control groups taken directly from the cited studies and are used to specify the direction and

relative ordering of network adaptations. These loops are semi-quantitative state models, not full ΔV_{margin} reconstructions, and no formal error propagation or global sensitivity analysis is performed on these data.

2.18.1 Common data-transfer scheme (R rules)

To project literature findings onto vCA1-centred loops we use four explicit transfer rules (Table 2.37):

Table 2.37 Data-transfer scheme

Code	Transfer rule	Neurophysiological rationale	Example in Results
R1	Identical cell population	Parameter measured in the same element (PV IN, AMPAR, etc.)	PV IN -30 % (Czeh et al. 2005)
R2	Shared θ/δ oscillation	Structures operate in-phase at 4–10 Hz	Glu/GABA shift (Mitsushima et al. 2013)
R3	Monosynaptic projection ($\times 0.7$)	Amplitude attenuation across a single synapse	Not used in the present model
R4	Global hormone / neuromodulator	CRF, cortisol, DA/NA reach all nodes systemically	Cortisol \uparrow (Schwabe and Wolf 2012)

Parameters measured outside vCA1 are marked with a dagger (\dagger) in Supplementary Tables S49–S51 and are transferred according to R1–R4 with $k = 1.0$ unless otherwise stated. No additional hidden scaling is applied.

2.18.2 Fear loop → schizophrenia-like trajectory

For the fear loop we construct a qualitative transfer matrix on the vCA1↔BLA↔dmPFC axis (Supplementary Table S49; Supplementary Discussion SD1). Literature-derived changes in medial-frontal Glx/GABA balance and redox/PNN/PV axis (R1), $\theta/4$ Hz mPFC–VTA–hippocampus coupling and $\theta-\gamma$ abnormalities (R2), γ/β synchrony (R1/R2), and chronic stress-induced morphological/epigenetic changes (R1) are encoded as discrete network states. The loop tracks the sequence:

neuromodulatory inputs (DA, cortisol) \rightarrow E/I shift \rightarrow redox load / PNN erosion \rightarrow PV dysfunction \rightarrow γ disorganisation \rightarrow dendritic retraction / synaptic consolidation,

which is directionally constrained by the cited work (SD1), without assigning a single ΔV_{margin} value.

2.18.3 Sadness loop → MDD-like trajectory

The sadness loop links vCA1 with sgACC/BA25 and default-mode network (DMN) nodes (Supplementary Table S50; SD2). We import reduced CSF HVA and elevated CSF CRF as global modulators (R4), local E/I tilt in sgACC/ACC from 7 T MRS (R1), redox/PNN/PV

vulnerability from prefrontal/hippocampal data (R1), and rumination-linked α/β changes and DMN \leftrightarrow sgPFC coupling (R2/R4). These are assembled into the ordered sequence:

monoaminergic/CRF bias \rightarrow sgACC E/I tilt \rightarrow redox/PNN/PV impairment \rightarrow altered α/β and DMN–sgPFC coupling \rightarrow dendritic/spine loss in PFC \rightarrow reduced executive control \rightarrow increased rumination,

as detailed narratively in SD2.

2.18.4 Trauma loop \rightarrow PTSD-like trajectory

The trauma loop is defined on the vCA1 \leftrightarrow BLA \leftrightarrow vmPFC axis (Supplementary Table S51; SD3). LC \rightarrow BLA noradrenergic bursts, dopaminergic modulation and CSF CRF elevation are treated as global R4 inputs; hippocampal glutamate increases and insular GABA decreases as local E/I shifts (R1/R2); stress-related PNN/PV changes as a γ -network fragility axis (R1); and vmPFC hypoactivity with α /fast-band abnormalities during trauma recall as oscillatory outputs (R4). Together they form the qualitative sketch:

trauma reminder \rightarrow NE/DA + CRF up-drive \rightarrow E/I shift (hippocampus/insula, E_{GABA} depolarisation) \rightarrow PNN erosion / PV dysfunction \rightarrow α suppression + fast-band abnormalities with vmPFC hypoactivity \rightarrow intrusive recollection \rightarrow renewed neuromodulatory bursts,

which specifies directionality and ordering rather than absolute magnitudes.

2.18.5 Practical rules for transfer to vCA1

Across all three loops we adopt the following conventions:

Oscillatory synchrony (R2).

Coherent 4–10 Hz activity between regions permits qualitative transfer of local $\Delta E/I$ and redox/PNN/PV state during those states.

Cellular identity (R1).

PV interneurons, PNNs and AMPAR-mediated synapses are assumed to follow broadly similar vulnerability and plasticity rules across limbic cortex; when the same element is involved, changes are transferred 1:1.

Neuromodulators (R4).

CRF, cortisol and catecholamines are treated as global gain-control signals and are applied uniformly ($k = 1.0$) to all nodes participating in the loop.

No extra numerical scaling.

Apart from the explicit R-rules (and the unused R3 heuristic), we do not introduce additional scaling factors when moving parameters from the literature into the loop diagrams.

2.18.6 Model limits and scope

- **Semi-quantitative nature.**
- The fear, sadness and trauma loops combine directionally consistent findings into ordered sequences but do not attempt a full dynamical-systems fit or a unified ΔV_{margin} estimate for each disorder.
- **Robustness to parameter variation.**

Qualitative testing indicated that varying individual inputs within plausible ranges ($\approx \pm 25\%$) does not change the order of events (e.g. E/I shift → redox load → PV/PNN changes → oscillatory and structural outcomes), nor the conclusion that chronic, biased engram re-activation can support SZ-, MDD- or PTSD-like trajectories.

- **Regional specificity and validation anchors.**

Morphological variables (e.g. dmPFC layer-III thinning, ACC grey-matter reduction) remain attached to their native regions and serve as validation anchors rather than direct inputs to vCA1.

- **Qualitative oscillatory markers.**

Indicators such as “ $\gamma \uparrow / \alpha \downarrow$ ” or altered $\theta - \gamma$ coupling are used as state labels only and are not quantitatively fitted.

These conventions keep the loop diagrams explicitly tied to Supplementary Tables S49–S51 and SD1–SD4, while clearly separating them from the fully quantitative ΔV_{margin} -based calculations in earlier sections.